



UNIVERSITÀ
DEGLI STUDI
DI PADOVA

UNIVERSITA' DEGLI STUDI DI PADOVA

Dipartimento di Ingegneria Industriale DII

Corso di Laurea Magistrale in Materials Engineering

Novel ink formulation to enable rapid debinding and sintering of alumina fabricated via vat photopolymerization

Relatore:

Prof. Giorgia Franchin

Correlatore:

Subhadip Bhandari

Laureanda:

Alice Nicolini

Matricola 2089923

Anno Accademico 2023/2024

Abstract

Vat photopolymerization is an additive manufacturing technology that allows the fabrication of complex ceramic structures with very high resolution, in the order of 10 – 100 μm . However, the bottle neck of the whole production process is represented by the delicate thermal debinding and sintering profiles required to obtain a dense and defect-free ceramics.

Herein, this work focuses on developing a novel ink formulation to produce dense alumina (Al_2O_3) parts with minimal defects. The goal was to obtain the highest possible solid loading while ensuring that the ink exhibited suitable rheological properties for the VP process. Camphor was used as a diluent to reduce the viscosity of the ink and facilitate both the printing and the debinding process. Several inks with varying Al_2O_3 content were prepared and characterized in detail to investigate their ability to produce defect-free components, with a particular focus on rheological behavior. The printed samples were first cleaned in water, then post cured, debinded (1 – 2 $^\circ\text{C}/\text{min}$) in argon and finally sintered in 60 s – 600 s using ultra-fast high temperature sintering (UHS), achieving a sintering time reduction of almost 99% compared to conventional sintering. The samples were sintered to very high relative density (up to 98%) without any noticeable defects.

This approach of shaping and sintering complex ceramic objects in few seconds has the potential to provide an energy-efficient alternative to conventional techniques such as pressureless sintering, hence representing a small step in the direction of addressing the current energy crisis.

Acknowledgements

I would like to express my deepest gratitude to Prof. Giorgia Franchin for the guidance and expertise provided over the course of this work. Special thanks to Prof. Paolo Colombo for giving his valuable feedback. I am also thankful to Subhadip Bhandari for his patience and feedback.

I would like to thank the University of Trento, in particular Prof. Vincenzo Sglavo, who allowed us to use the UHS equipment, and Dr. Mattia Biesuz, who coordinated and arranged the collaboration.

Another thanks goes to my family, who has always supported me, and to my best friends, Katia and Sofia, who have helped me stay motivated and in high spirits. Lastly, I would like to acknowledge all the friends who have stayed by my side throughout these years.

Contents

Chapter 1	6
1.1. Additive Manufacturing of Ceramics	6
1.1.1. Vat photopolymerization	8
1.1.2. The printer	10
1.2. Ink formulations for vat photopolymerization	11
1.2.1. The ceramic powder	13
1.2.2. The monomer	14
1.2.3. The photoinitiator	14
1.2.4. The dispersant	15
1.2.5. The diluent	16
1.3. Printing	16
1.4. Post-processing	17
1.4.1. Debinding	18
1.4.2. Sintering	19
1.5. Typical defects of ceramics fabricated through VP	22
1.6. Goal of this work	23
Chapter 2	25
2.1. Materials	25
2.2. Preliminary analysis	26
2.3. Preparation of the ink	27
2.4. Printing	28
2.5. Post-processing	30
2.6. Characterization	32
Chapter 3	34

3.1.	Preliminary analysis.....	34
3.2.	Rheological characterization.....	36
3.2.1.	Effect of the ceramic loading.....	36
3.2.2.	Effect of dispersant.....	38
3.2.3.	Effect of the monomer.....	39
3.2.4.	Effect of camphor.....	40
3.2.5.	Effect of the ball milling time.....	41
3.3.	Printing.....	42
3.4.	Thermogravimetric analysis.....	43
3.5.	Post processing.....	44
3.5.1.	Cleaning solvent.....	44
3.5.2.	Post-curing time.....	44
3.6.	Debinding and sintering.....	46
3.6.1.	Shrinkage.....	46
3.6.2.	Density.....	49
3.6.3.	X-ray diffraction.....	50
3.6.4.	SEM of debinded samples.....	51
3.6.5.	SEM of the conventionally sintered samples.....	52
3.6.6.	SEM of UHS samples.....	56
	Conclusion.....	60
	Outlook.....	61
	Bibliography.....	62

Chapter 1

Additive Manufacturing

1.1. Additive Manufacturing of Ceramics

Ceramics are inorganic, non-metallic materials that generally exhibit high hardness and stiffness, good resistance to high temperatures and excellent chemical inertness [1], [2]. Their discovery dates back thousands of years and they have been produced in various forms and functions over the course of all human history. Despite this, significant innovations have been few and far between until last century, when unprecedented advancements in materials science resulted in the development of a new class of ceramic materials: advanced ceramics [3], [4]. They were created to be exploited in applications related to aerospace, automobile, transport, energy, defense and communications, and for this reason they possess superior mechanical properties and corrosion resistance, as well as electrical, magnetic and optical properties that can be tailored and adapted for a broad range of applications [1], [2].

The main drawback of advanced ceramics is their tendency to exhibit low toughness and low ductility (high brittleness), which combined with the high hardness and high melting temperatures makes them difficult to process, even more so when an application requires components with complex structures [1], [3].

Traditional ceramic processing technologies such as slip casting, tape casting, injection molding, die pressing, etc. allow to shape raw materials into a green body that can then be sintered at high temperatures to achieve densification and gain suitable mechanical properties [5]. These techniques present significant limitations in terms of design, long processing times and high costs. Molds cannot produce structures with high geometrical complexity and tend to be extremely expensive, thus requiring large volumes of production to amortize costs [3], [5]. Machining is rarely employed in the manufacturing of ceramics due to their hardness, brittleness and high crack sensitivity. The risk of introducing defects is high and the advanced cutting tools required to carry out the process are subjected to severe wear, resulting in significant expenses [1], [5].

These problems could be addressed with additive manufacturing (AM), also known as 3D printing. AM is defined by the ISO/ASTM standard 52900:2021(E) as the “process of joining materials to

make parts from 3D model data, usually layer upon layer, as opposed to subtractive manufacturing and formative manufacturing methodologies” [6]. This revolutionary approach enables the fabrication of near-net-shape ceramic parts with complex geometries that are impossible to produce with traditional ceramic processing methods [1], [5]. Furthermore, the design of the manufactured components can be modified with ease without any physical intervention on the machine because no expensive tooling is required [1]. As a result, the manufacturing cost-per-piece is almost constant, independently from volume of production and shape complexity, and only related to the material use, machine power consumption and cost of labour [1], [7]. These characteristics make AM a particularly attractive alternative to traditional shaping technologies, especially for small production volumes such as prototyping [1].

From the economical point of view, AM involves higher automation, less tooling and shorter supply chains, therefore it could generate significant cost savings and reduce energy demands and CO₂ emissions compared to traditional manufacturing processes. The highly complex structures achievable through AM could also allow for significant savings during the use phase of a product, especially in the fields of transport and aerospace: replacing a dense component with one with a porous structure reduces the overall weight of a machine and leads to savings in terms of fuel consumption [8].

Several ceramic AM technologies have been developed so far, which can be classified according to different criteria. Depending on the type of feedstock used for printing it is possible to distinguish slurry-based, powder-based and bulk solid-based methods [5]. Another criterion distinguishes between multi-step processes, which result in the formation of a green body that needs to undergo thermal treatments in order to be transformed into the functional ceramic component, and single-step processes, which are able to shape and sinter the ceramic in one step [1]. A brief summary of current ceramic AM technologies can be seen in Table 1.1.

Table 1.1: Summary of ceramic AM technologies [1].

	Family	Feedstock	Description/shaping method
Multi-step	Vat photopolymerization	Photocurable ceramic slurry or photocurable preceramic polymer	The liquid feedstock is selectively cured through light-activated polymerization
	Material Jetting	Ink or suspension of ceramic particles	Droplets of ink are selectively deposited on a substrate.
	Material Extrusion	Ceramic-loaded paste, ceramic-loaded filament or preceramic polymer filament	The feedstock is extruded through a nozzle and deposited on a platform layer-by-layer
	Powder Bed Fusion	Powder bed of ceramic particles mixed with a polymer or binder	A concentrated heat source (Laser) melts the binder and joins the particles together
	Binder Jetting	Powder bed of loose ceramic particles	Droplets of liquid binder are selectively deposited on the bed of powders
	Sheet Lamination	Thin sheets of material	Sheets are cut by laser, stacked and joined
Single-step	Directed Energy Deposition	Ceramic particles	Ceramic particles are fed from a nozzle into the focal point of a laser beam; they melt and then solidify on a substrate
	Direct Laser Sintering	Powder bed of loose ceramic particles	A concentrated heat source (Laser) sinters the particles together

1.1.1. Vat photopolymerization

Vat Photopolymerization (VP) is defined as “an additive manufacturing process in which a liquid photopolymer in a vat is selectively cured by light-activated polymerization” [6]. VP stands out among the other families of ceramic AM technologies because it allows high resolution in the order of 10-100 μm [5]. It also has the added benefit of being one of the most established processes in the AM market, established and commercialized at industrial level [1], [7].

The main steps to produce a dense ceramic object with VP include designing the 3D model, printing and post-processing (including cleaning, debinding and sintering) [1]. An overview of the whole process has been schematized in Figure 1.1. The desired geometry is designed with a CAD software

and then it is processed by a slicing software that slices the 3D model into 2D layers. The printer can only read this sliced file.

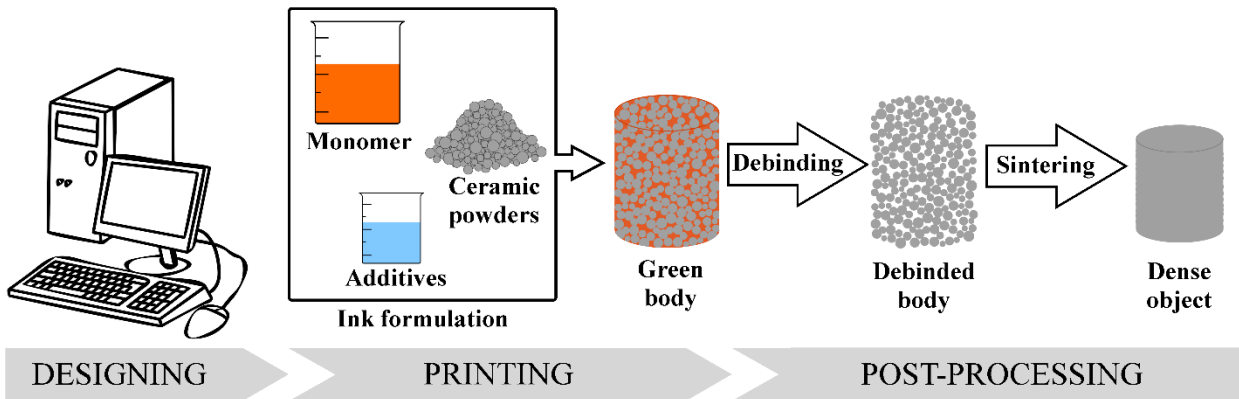


Figure 1.1: Schematic representation of the main steps required to produce a ceramic object through VP.

An ink for vat photopolymerization typically consists of ceramic particles suspended in a photocurable polymeric resin [9]. After it is prepared and poured into the vat of the printer, the ink is selectively exposed to UV light and cured, usually in a matter of seconds. The object is manufactured layer-by-layer, progressively building a stack on a printing platform until the green body with the desired geometry is obtained [7].

Post-processing consists of several steps, with the exact number of steps varying according to the specific case. For instance, cleaning off the residual ink from the printed body and performing the thermal treatments to transform the green body into the final object are essential procedures for obtaining a high quality dense ceramic object, while other operations such as removing support structures and polishing to improve surface finish are not always necessary [7].

Advanced ceramics that have successfully been fabricated through VP are silica (SiO_2) [10], alumina (Al_2O_3) [11], [12], hydroxyapatite [13], zirconia (ZrO_2) [14], silicon oxycarbide (SiOC) [15] and silicon nitride (Si_3N_4) [16]. Other materials such as SiC and TiC tend to be more challenging to manufacture through photopolymerization-based AM technologies due to the excessive scattering and absorption of light, which result in poor resolution and insufficient curing [1], [3].

The limited selection of ceramic materials that can currently be printed is one of the main drawbacks of VP, together with the use of photopolymers which are generally toxic and not environmentally

friendly [17]. Another limitation is the maximum wall thickness that can be manufactured without formation of defects during the subsequent thermal treatments [1], [10].

1.1.2. The printer

A printer for VP consists of three main parts: a light source, a printing platform (also called build head) and a vat for the photocurable resin [7].

There are two possible configurations of the printer (Figure 1.2):

- *Bottom-up configuration*: the light source is beneath the vat, which has a transparent bottom to allow light to pass through, and the build head is dipped in the resin from above. The layer thickness is equal to the immersion height, that is the distance between the head and the bottom of the vat. The resin trapped between them is exposed to light for a defined exposure time, then the head moves upwards, creating a vacuum that helps recoat the bottom of the vat with new unpolymerized resin. The separation of the cured layers from the vat is a critical step because they risk to detach from the build head [7].
- *Top-down configuration*: the light source is mounted above the vat and the build head is always completely immersed in the resin. The layer thickness is equal to the building platform depth, that is the distance between the head and the surface of the liquid resin. This thin layer is cured by light and adheres to the build head, which then moves downward into the vat to make space for a new layer. A recoating blade may be necessary to help distribute the new layer of resin in the space that was vacated. While this configuration has no issues regarding adherence between the cured resin and the vat, the contact between atmospheric oxygen and resin at the free surface may inhibit polymerization. Furthermore, a larger amount of resin is required to operate and part height is limited by the depth of the vat, unlike in the bottom-up approach [7], [18].

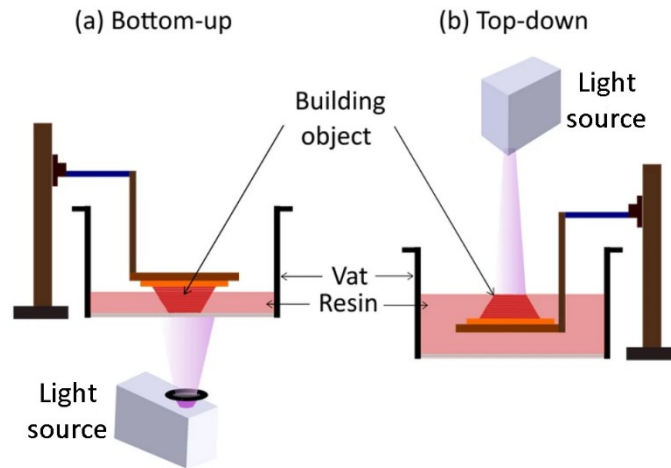


Figure 1.2: Possible configurations of a VP printer [7].

1.2. Ink formulations for vat photopolymerization

In general, an ink for ceramic vat photopolymerization consists of the ceramic powder, monomer, photoinitiator (PI) and several other additives such as diluents and dispersant that may be added to improve the rheological properties of the suspension [9], [19].

The fundamental characteristic of such an ink is its ability to undergo photopolymerization upon exposure to light: UV radiation is absorbed by the PI, which gets activated and generates reactive species able to attack the functional groups of the monomer and initiate the polymerization reaction [7]. Long macromolecules are produced by continuous addition of monomers, converting the liquid resin into solid polymer in a few seconds. If monomers are multifunctional, cross-links can form between macromolecular chains, generating a 3D network [19].

This polymeric network acts as a matrix that binds the ceramic particles together and provides strength to the green body. This polymeric network will be later removed through the debinding step, while sintering will allow to obtain a dense ceramic part with suitable mechanical properties [19].

The rheological characteristics of the ceramic suspension instead affect the recoating process during printing. Inks for VP generally exhibit strongly non-linear rheological behavior due to the presence of the dispersed solid phase [9]. Shear-thinning behavior, characterized by a decrease in viscosity when the shear rate increases [20], is common for suspensions with low to moderate solid loadings and ideal for a VP process [9]. It is caused by deflocculation and arrangement of the particles into streamlined layers when shear rate is increased [21]. Conversely, highly loaded ceramic suspension might exhibit shear-thickening behavior, that is higher viscosity with increased shear rate [20], due to the formation of agglomerates as a result of decreasing inter-particle distance. [21].

The rheological behavior of a fluid can be described by the Herschel-Bulkley model [22], [23]:

$$\tau = \tau_0 + k\dot{\gamma}^n \quad (1)$$

τ is the shear stress, τ_0 is the yield stress, k is the consistency index, $\dot{\gamma}$ is the shear rate and n is the flow behavior index. The difference between 1 and the parameter n , which is a characteristic constant of the fluid, allows to quantify the non-Newtonian behavior of a fluid. Values of n comprised between 0 and 1 correspond to a shear thinning behavior, while n higher than 1 is related to shear thickening behavior. The type and amount of monomer and dispersant, along with the solid loading, the particle size and size distribution all affect the overall behavior of the ink [9].

Another characteristic that is strongly related to the rheology is the stability of the suspension. An ink for VP must be homogeneous and stable for extended periods (in case it has to be stored), so as not to have concentration gradients in printed parts [9]. The main phenomena responsible for an unstable suspension are sedimentation due to gravity and flocculation due to interparticle attraction [24]. The effect of sedimentation can be considered negligible due to the high solid loading and small particle size typical of VP formulations [9], [25], therefore flocculation is the main destabilization mechanism, leading particles to form large aggregates that sediment faster [9].

The suitable viscosity for printing depends on the configuration of the printer, and should be less than 20 Pa·s at a shear rate of 100 s⁻¹ at 25 °C for devices equipped with recoating devices and less than 3 Pa·s at 30 s⁻¹ for printers without recoating blade [7], [11]. The viscosity of a ceramic suspension decreases when temperature increases, but this characteristic is difficult to exploit in practice because printers would need to be more complex to include temperature control and the resins should be free of volatile organic components [9].

To summarize, the requirements that a formulation for ceramic VP must satisfy are:

- Low viscosity: the ink must easily flow and form uniform and thin layers (typically with thickness comprised between 25 and 100 μm) to produce complex geometries within a reasonable processing time [9], [19].
- Shear thinning behavior, to facilitate the recoating process [19].
- Transparency to the wavelengths of light used for photopolymerization (which are generally in the UV range), to ensure sufficient light penetration through the resin and uniform curing [19].
- High solid loading, to reduce shrinkage and achieve high density and mechanical properties after sintering [7].

1.2.1. The ceramic powder

It is desired to have a solid loading as high as possible in order to accelerate the debinding process, minimize the resulting porosity and reduce shrinkage during sintering, thus preventing excessive deformations and cracking and obtaining dense and homogeneous ceramic parts [19]. Ideally, the ceramic loading should be higher than 40 vol.% to avoid defects during post-processing [7].

However, increasing the solid loading severely affects the rheological behavior of the suspensions, specifically causing a higher viscosity or a transition from shear-thinning to shear-thickening behavior [9]. This is in contrast with the necessity to have a low viscosity to facilitate the recoating process. The common solution is to employ additives such as dispersants that help reduce the viscosity of the suspension while maintaining a sufficiently high ceramic loading [1], [9], [19].

Particle size and size distribution are also important parameters to consider when the suspension is highly loaded. Fine powders result in higher viscosity than coarse ones and are more prone to agglomeration due to their large surface area. The effect of size distribution is instead more complex: on one hand, suspensions with broader particle size distribution may be more fluid, because small particles can flow in between larger ones [9], [25]; on the other hand, using nanometric particles can increase the viscosity of the fluid around bigger particles, reducing the rate of sedimentation and improving suspension stability at the expense of fluidity [9].

The ceramic particles have a negative influence on the curing characteristics as they affect the optical properties of the suspension. Powders attenuate light by scattering, which reduces light penetration inside the ink and significantly worsens the lateral resolution and the overall printing accuracy [7], [19]. The extent of light scattering in a ceramic suspension depends on several parameters, namely the ceramic loading and the particle size. Higher solid loading as well as finer particles lead to more scattering. The most important parameter that affects scattering however is the difference between the refractive index (RI) of the ceramic material and the RI of the liquid medium: the higher the mismatch, the more pronounced scattering will be [7], [19].

Taking into consideration all of the above, it is possible to formulate the following requirements that a ceramic material has to satisfy in order to be suitable for a VP process [19]:

- The refractive index (RI) must be as close as possible to that of the monomer, to minimize scattering and have a better control of the polymerization process [7].
- The ceramic must exhibit low absorption of light in the UV range, to have adequate penetration depth and maintain sufficient light energy to initiate photopolymerization.

- The median particle size (D_{50}) has to be smaller than the layer thickness (25 μm to 100 μm) to improve vertical resolution, but not so small as to negatively affect the properties of the suspension. The recommended particle size is between 0.05 μm and 10 μm [19].

1.2.2. The monomer

There are several aspects that need to be taken care of when choosing a particular monomer. Firstly, the viscosity of the suspension is proportional to the viscosity of the monomer, therefore it should be as low as possible [9].

The next important characteristic is the functionality of the monomers, which play a fundamental role during polymerization. Multifunctional monomers promote crosslinking, which increases the strength of the green body, but also result in higher viscosity than monofunctional monomers [26]. This issue can be solved by adding to the formulation inert diluents to help reduce viscosity [9].

The most used monomers for the preparation of formulations for ceramic VP are acrylates and epoxy resins [9]. Compared to aqueous formulations, these resins display greater cured depth and better mechanical properties of the green bodies, but their viscosity is higher and they are generally hydrophobic, therefore they have low affinity for ceramic particles. The use of dispersants is necessary to ensure that non-aqueous suspensions have a suitable rheological behavior for VP [9], [19].

Acrylate-based formulations are crosslinked via free radical photopolymerization [27] while epoxy-based resins cure through ionic photopolymerization [28]. Acrylates are more reactive and cure more quickly, but tend to suffer from shrinkage and warping and may be affected by environmental oxygen. Epoxy-based resins instead cure slowly, so the risk of defects is lower, and reaction is unaffected by oxygen. Their compounds tend to be less toxic than acrylates. However, only a small number of epoxy-based resins is available compared to acrylate-based alternatives, so they are rarely used [7], [28].

1.2.3. The photoinitiator

Photoinitiators (PI) are low-molecular-weight compounds that can produce reactive species when interacting with light [19]. The absorption of a photon with sufficient energy causes the promotion of an electron to an excited state. The excess energy is released when the PI returns to the original ground state, causing the formation of free radicals or ions that can attack the functional groups of the

monomers. PIs are a necessary ingredient in the formulation of an ink for VP because most monomers are unable to generate reactive species and initiate polymerization by themselves [7], [19].

The PI strongly affects the monomer-to-polymer conversion and the curing depth. Low PI concentrations result in a conversion to polymer insufficient to cause solidification of the liquid ink and a curing depth that approaches zero. Conversely, extremely high PI concentrations cause a significant reduction in the light penetration depth and therefore in the curing depth because of high light absorption. The optimal concentration of PI has to be evaluated for each formulation so as to maximize the curing depth [19].

1.2.4. The dispersant

Dispersants are often used for several reasons, including the stabilization of ceramic suspensions, breaking up of agglomerates and prevention of sedimentation [9], [19].

There are three main types of dispersion mechanisms for ceramic particles in a liquid:

- Electrostatic stabilization, which is based on the repulsive electrostatic potential generated when ions in the liquid are attracted to the electrically charged surface of the ceramic particles. This repulsive potential decreases with the distance from the particle surface and is proportional to the dielectric constant of the suspension medium, therefore effective electrostatic stabilization can only be achieved in aqueous suspensions [20]. Even then, it might be insufficient to fully stabilize the suspension [9].
- Steric stabilization, that occurs when long organic molecules are adsorbed on the surface of the powders. When the polymeric layers of two adjacent particles overlap, a repulsion force is generated, preventing aggregation [20]. Unlike the previous method, steric stabilization is also effective for non-aqueous suspensions. If the ceramic particles have hydrophilic surfaces, the dispersant must have hydrophilic groups to anchor on the particle surface and hydrophobic chains soluble in the non-aqueous medium. A good steric dispersion requires complete coverage of the particle surface by a steric layer of sufficient thickness, a strong affinity between ceramic and dispersant to ensure a strong attachment and a high affinity between the dispersant and the solvent medium [9], [29].
- Electrosteric stabilization, which combines the previous methods thanks to the use of polyelectrolytes, which are polymers with charged species along their chain that can promote

both steric barrier and electrostatic potential [20]. This mechanism yields the best results in aqueous suspensions [9].

The optimal amount of dispersant is proportional to the superficial area of the ceramic powders. Low amount of dispersant can result in incomplete coverage of the particles, which could then aggregate. On the contrary, a large amount of dispersant increases the viscosity of the suspension because the excess is dissolved in the medium [9].

Commercial dispersants for VP formulations usually possess highly polar functional groups such as amine, carboxyl, silane or phosphoric acid groups [9]. Since the exact effect on rheology depends on their chemical structure, on the specific ceramic powders and on the composition of the monomer, the optimal amount of dispersant has to be carefully evaluated for each formulation [19].

1.2.5. The diluent

Diluents help lower viscosity and can improve the optical properties, reducing the difference in RI between monomer and ceramic particles without modifying the reactivity towards UV light [30]. Inert diluents do not participate in the photopolymerization reaction and do not contribute to the mechanical properties of the green printed parts, but contribute to the reduction of the polymerization shrinkage and the resulting residual stresses. These additives are commonly employed when the solid loading exceeds 40 vol% to manage the rheological behavior of the ink [9], [19].

Some diluents, such as polypropylene glycol or polyethylene glycol, also have an important role during debinding: as the first non-ceramic component to evaporate, they create a network of open porosities in the green body that facilitates the subsequent diffusion and expulsion of the pyrolyzed resin, preventing the formation of cracks [31].

Some other examples of diluents that have been used so far are water and glycerol [9]. Camphor was explored as a novel diluent in a study by Lee et al. [32], which demonstrated it significantly decreases the viscosity of the resin without deteriorating the photopolymerization behavior. This makes camphor an excellent inert diluent for an ink for VP.

1.3. Printing

Vat photopolymerization is used to selectively cure the ink and transform the liquid feedstock into a solid green body through a layer-by-layer approach.

One of the most important parameters is the curing depth, which is the maximum thickness that can effectively be cured when the ink is exposed to a light of a determinate intensity. It is recommended that the curing depth should always be slightly higher than the layer thickness (which varies in the range of 10 - 200 μm), to ensure good interlayer bonding [19].

Another important parameter is the exposure time of each layer to the light. If it is too short, the photopolymer is undercured and may dissolve in the solvents during the subsequent cleaning operation. On the other hand, if exposure time is too high it may lead to strong adhesion between the cured layer and the vat base, possibly damaging the vat base over time [7]. Overcuring also worsens the lateral resolution of the printed part [19].

In bottom-up configuration, if the adhesion force between the newly cured layer and the bottom of the vat is stronger than that between the layer and the build platform (or the previously cured layers), when the build head lifts the cured polymer will detach from it and remain in the vat. There are two ways to solve this problem: minimize the adhesion force between the bottom of the vat and the printed layer, which is affected by the material of the transparent film as well as the composition of the ink, or maximize the adhesion between the first printed layer and the building platform. The latter can be achieved by roughening the surface of the platform before printing and by a careful choice of the printing parameters [11].

1.4. Post-processing

Post-processing is the last stage of production of a ceramic through AM. The most common operations that may be carried out in this stage are:

- Detaching the sample from the print head
- Cleaning of the residual photocurable ink
- Removal of support structures
- Post-curing
- Thermal treatments

When the printed object finally emerges from the vat, it is covered in uncured resin, which needs to be immediately cleaned off [33]. A variety of solvents can be used to rinse or sonicate the parts, but the choice has to be compatible with the prepared ink formulation. Highly reactive solvents such as isopropyl alcohol, ethyl alcohol or acetone, while effective, may wear off the surface of the printed

object and ruin the surface quality [34], [35]. Submerging the green bodies into these solvents might also cause swelling and affect the final geometry [7], [35].

Post-curing the printed parts in an UV chamber is performed to ensure complete polymerization and thus improve the mechanical properties of the green body [36]. The degree of conversion, that is the extent to which the resin has reacted and transformed into a solid polymer, is generally low in the printed bodies due to the short curing times employed in VP. At the beginning of the reaction the monomers are in a liquid-like, high mobility state and can easily diffuse and promote polymerization, however, as soon as the polymer network starts to form their mobility decreases significantly. This point is usually reached in a few seconds and afterwards it is more difficult for monomers to diffuse and react with other monomers, so the overall degree of conversion remains low [37].

Post-curing increases the degree of conversion of the printed bodies, enhancing material properties and dimensional accuracy. It must be done with consideration of the thickness of the walls of the printed objects: if too thick, radiation will not be able to penetrate and reach the inner parts, leading to anisotropy in the degree of polymerization across the wall thickness. Such anisotropy could cause deformations during later operations [7]. The exposure time during post-curing also affects the mechanical properties of the printed part [37].

Once the printed parts are cleaned and (if necessary) post-cured, they are ready for the thermal treatments, which are considered as the most critical step in the whole manufacturing process and have the biggest impact on the final properties of the ceramic body. Hereafter they will be discussed in detail.

1.4.1. Debinding

The first thermal treatment to which the green body is subjected is the thermal debinding. During this process, the crosslinked polymer which acts as matrix for the ceramic particles is decomposed and evaporated at high temperatures. The removal of the organic fraction causes shrinkage, reduction in weight and formation of porosity. The end result is a very porous and fragile structure that still needs to be sintered to obtain a densified ceramic part [7].

The atmospheric conditions affect the type of decomposition process that happens when the green bodies are heated. Debinding in air, organics undergo rapid oxidative decomposition, often leading to violent exothermic reactions, which increases the possibility of generating internal stress that might lead to cracks or deformation. Instead, debinding in inert environments, such as argon or vacuum, the

pyrolysis occurs through the thermolysis of chemical bonds and is therefore endothermic. As a result, the debinded bodies often appear gray or brown [38].

The shape of the green body also has a significant influence on the debinding process. The higher the surface-to-volume ratio of the structure, the easier it will be for the pyrolyzed products to get out of the structure [31]. For this reason, thin or porous structures are easier to process than parts with large wall thickness. Furthermore, smaller parts are easier to debind than bigger ones. The specific geometry has to be considered when optimizing the process [31], [39].

Nonetheless, the debinding step is critical to determine the quality of the final ceramic part. Incorrect parameters such as too high heating rate or inappropriate holding temperature may generate in the body defects that will be impossible to remove during the following sintering process [40].

1.4.2. Sintering

Sintering is the final stage of post-processing, during which the debinded body is treated at very high temperatures to obtain a dense structure [7]. It's an energy intensive process and consumes the biggest fraction of energy required for processing ceramics [4].

Fundamental phenomena that occur during a sintering process are the formation of bonds between the ceramic particles, the removal of porosity, and grain growth, which ideally result in the shrinkage and densification of the ceramic body [41].

The driving force of sintering is the reduction of the free energy of the system, which is achieved by reducing the surface free energy through the formation of grain boundaries and elimination of solid-air interfaces. Particles have large surface-to-volume ratios which correspond to high surface energy. Compaction of the powders and reduction of porosity is achieved through the diffusional transport of matter along definite paths called the *mechanisms of sintering* (Figure 1.3): surface diffusion, volume diffusion from the surface and vapor transport (which are non-densifying mechanisms), grain boundary diffusion, volume diffusion from the grain boundary and plastic flow by dislocation motion (which are instead densifying mechanisms). They all lead to the growth of necks between the particles, but only densifying mechanisms lead to densification and pore removal [41].

Sintering is thought to occur in three stages. The initial stage consists of fairly rapid neck growth in between the particles. The intermediate stage involves densification by reduction of the cross-section of the pores, which at this point can be envisioned as a continuous phase along grain edges. This stage covers the major part of the sintering process and ends when the pores become unstable and turn into

isolated porosities. The final stage of sintering consists of continuous shrinkage of the remaining pores, that might even be completely eliminated [41].

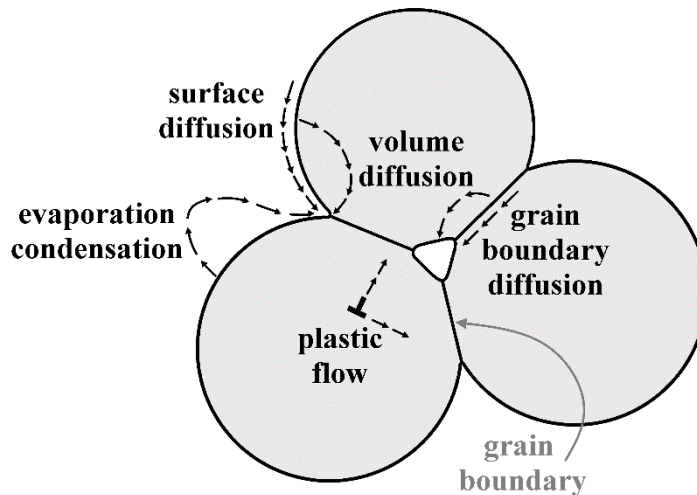


Figure 1.3: Mechanisms of sintering [42].

Coarsening is the occurrence of both grain growth and pore growth. It is generally an undesirable phenomenon because it reduces the driving force for densification by providing an alternate route through which the energy of the system can be lowered: the reduction of the total grain boundary area. Coarsening mostly occurs in the earlier stages of sintering, although grain growth is also pronounced in the final stage [41].

Since densification occurs by the flow of matter, it is rapid when the diffusion distance is short, therefore a smaller grain size is desired. Rapid grain growth causes the reduction of the densification rate, making longer sintering times necessary to reach the required density. For this reason, it is possible to talk about a competition between sintering (densification) and coarsening [41], [43].

The properties of the final ceramic object are strongly dependent on its microstructure: the grain size and shape, the amount, size and distribution of pores and the presence of eventual secondary phases. Better mechanical properties are associated to higher density, smaller grains and homogeneous microstructure. The characteristics of the initial powders, the forming method and the structure of the green body strongly influence the final microstructure and therefore need to be carefully controlled to obtain the desired properties [41].

When no external pressure is applied to the body the process is referred to as *conventional* or *pressureless sintering*. Conversely, *pressure sintering* refers to a process during which external pressure is applied [41].

Conventional sintering is much more economical than pressure sintering and for this reason it is the most used method. The main process variables are the heating cycle and the sintering atmosphere. The most common heating schedule consist of an initial heating ramp until a fixed sintering temperature is reached, an isothermal hold at this temperature for a determinate time and a final cooling down to room temperature [41].

Bigger parts require slower heating ramps in order to avoid temperature gradients between the core and the outer layer. However, the heating rate has a significant effect on the microstructure: coarsening activates more easily than densification at lower temperatures, so a faster heating rate allows to bypass this unfavorable region and enhances densification during the isothermal temperature hold, resulting in a finer microstructure [4], [41].

Control of the sintering atmosphere instead is important for controlling processes such as decomposition, evaporation of volatile constituents and vapor transport. The use of vacuum can improve the final density by removing gases trapped inside the structure that might otherwise hinder the final stages of densification or cause swelling [41].

Recent years have seen an increasing push for more environmentally friendly processes to reduce the carbon footprint and prevent the climate crisis. Strategic sectors such as the aerospace and nuclear industries have been demanding advanced ceramics either showcasing enhanced functional properties or capable to withstand extreme conditions of temperature and stress, not achievable with conventional sintering. The combination of these factors has prompted researches to look for alternative technologies [4].

Ultrafast High-temperature Sintering (UHS) is a very recent development that was first reported by Wang et al. in 2020 [43]. This technique features extremely high heating rates of 10^3 to 10^4 °C/min, high cooling rates up to 10^4 °C/min and high sintering temperatures up to 3000 °C in inert atmosphere. These features allow to achieve very short sintering times, of the order of 10-60 s. The green body is sandwiched between carbon felt which is Joule heated by an electric current. The heat generated in the felt is then transferred to the sample, mainly by radiation. The parameters influencing the UHS process include the current (or the power) and the hold time. The temperature profile can be tuned by varying the current (or the power) to control the sintering process and the microstructural evolution of the ceramic pieces [43].

The short sintering time of UHS helps prevent evaporation of volatile species and unwanted interdiffusion at the interfaces of multilayer structures, reducing or eliminating segregations and defects at grain boundaries. UHS is also compatible with complex 3D printed structures because the sample can be easily placed in the carbon felt irrespective of its geometry and complexity [43].

As previously mentioned, sintering involves a competition between the coarsening and densification of particles. The former tends to dominate at low temperatures due to the prevalence of surface diffusion, while densification prevails at high temperatures where diffusion at grain boundaries and bulk is more important. Since the ultrahigh heating rates of UHS bypass the low temperature region, the coarsening of particles is reduced while maintaining the driving force for sintering, resulting in dense ceramic bodies with grain sizes that are usually smaller than parts sintered through traditional methods [43].

The combination of AM and UHS could provide an energy-efficient alternative to conventional manufacturing processes that drastically reduces the production time while maintaining a good quality of the obtained components [44].

1.5. Typical defects of ceramics fabricated through VP

Optimization of the process parameters and control of the defects is important to improve the quality and performance of the manufactured ceramics [45].

The most common type of defect is porosities, which greatly affect the density and mechanical properties and might originate other defects, such as cracks. Porosities are usually generated after debinding and can be reduced by an optimized sintering process. Pores can also originate from air bubbles incorporated into the slurry during its preparation and trapped into the green body after curing [45].

Delamination is a defect typical of AM due to the principle of layer-by-layer manufacturing [45]. Their formation can be attributed to two main causes:

- Low polymerization between layers and insufficient interlayer bonding strength, due to inadequate light penetration or low exposure time during printing [45].
- Failure of the interlayer junction due to tensile stresses applied perpendicularly to the layers. Such stresses may be generated by differential thermal shrinkage between surface and core of a body during the thermal treatments [45], by pressure gradients created by the escaping gases

during debinding [38], by high separation forces when detaching the cured layer from the vat bottom (in VP with bottom-up configuration) [45] or by polymerization shrinkage [11].

In the worst cases, these phenomena might also lead to the formation of cracks, which cannot effectively be eliminated and make the component unsuitable for application [45].

Several precautions can be taken to prevent delaminations and cracks: the composition of the ink and printing parameters need to be optimized; suitable additives must be added to facilitate gas expulsion during the debinding stage; the parameters of the thermal treatments have to be carefully controlled, usually through slow heating rates and optimization of the temperature profile. [45].

Cracks and delaminations are also conditioned by the shape of the piece: wall thicknesses greater than 10 mm are more likely to experience defect formation during debinding [39], [45].

The “staircase effect” is another characteristic defect of AM, which refers to the presence of ridge-like defects on the surface of the part due to the stacking of different layers and light scattering. It can cause stress concentration when an external load is applied and anisotropic behavior between the build orientation and other directions. Specifically, failing is more likely to occur when the load is applied in the building direction. [45].

Other possible defects that can manifest in additively manufactured pieces are:

- Warpage and deformations, which are generally caused by non-isotropic shrinking during sintering [31] and residual stresses [45];
- Compositional defects, such as impurities deriving from unwanted reactions during the thermal treatments [45];
- Structural collapse, which may be caused by excessive shrinkage during firing [46].

1.6. Goal of this work

After a careful consideration of the literature data summarized above, it was decided to focus this project on the development of a formulation that allowed the fabrication of high-quality alumina (Al_2O_3) components through vat photopolymerization. In particular, the goals were:

1. To prepare an ink with high solid loading (> 50 vol%).
2. To test the effectiveness of camphor as an inert diluent.

3. To produce samples that could undergo rapid debinding and sintering treatments, thus achieving a time- and energy-efficient process.
4. To evaluate the compatibility of VP with the new Ultrafast High-temperature Sintering technology, to further improve the efficiency of the manufacturing process.

Chapter 2

Materials and methods

2.1. Materials

The ceramic powder used in this thesis consists of commercial α -Al₂O₃ powder (CT 3000 LS SG, Almatiss) with 99.8% purity, specific surface area equal to 7.80 m²/g and median particle size (D₅₀) of 0.5 μ m.

Several difunctional monomers were examined to optimize the ink formulation: 1,6-hexanediol diacrylate (HDDA), tetra(ethylene glycol) diacrylate (TEGDA) and two types of poly(ethylene glycol) diacrylate (PEGDA) with average molecular weight of 250 g/mol and 575 g/mol respectively (PEGDA250 and PEGDA575). All chemicals were sourced from Sigma Aldrich. Some of the most important properties relating to the monomers are reported in Table 2.1, while their chemical structures are shown in Figure 2.1.

Bis(2,4,6-Trimethylbenzoyl)phenylphosphine oxide (Omnirad 819, IGM resins) was chosen as photoinitiator. It allows radical polymerization upon UV exposure and according to the producer it is especially suitable for white pigmented formulations.

BYK-111 (BYK Chemie GmbH), a copolymer dispersant containing carboxyl and ester groups, was used in order to ensure homogeneous dispersion of the ceramic particles in the suspension. This phosphoric acid ester-based wetting and dispersing agent provides deflocculation through steric stabilization [47].

To reduce the viscosity of the suspension and obtain inks with high solid loading, camphor (C₁₀H₁₆O) was added to the formulation as an inert diluent. Its chemical structure is reported in Figure 2.2. Our camphor was acquired from Il Regno Vegetale (Italy).

Water, acetone, ethanol, isopropanol, 2-phenoxyethanol (TCI) and propylene carbonate (TCI) were evaluated as solvents to clean the samples after the printing process.

Table 2.1: Average properties of the monomers considered in this study [9], [48].

Monomer	Molar mass [g/mol]	Density [g/mL] at 25 °C	Viscosity [mPa·s]	Refractive index [-]
HDDA	226	1.01	5–10	1.456
PEGDA 250	250	1.11	15–50	1.463
PEGDA 575	575	1.12	57	1.467
TEGDA	302	1.11	5–30	1.465

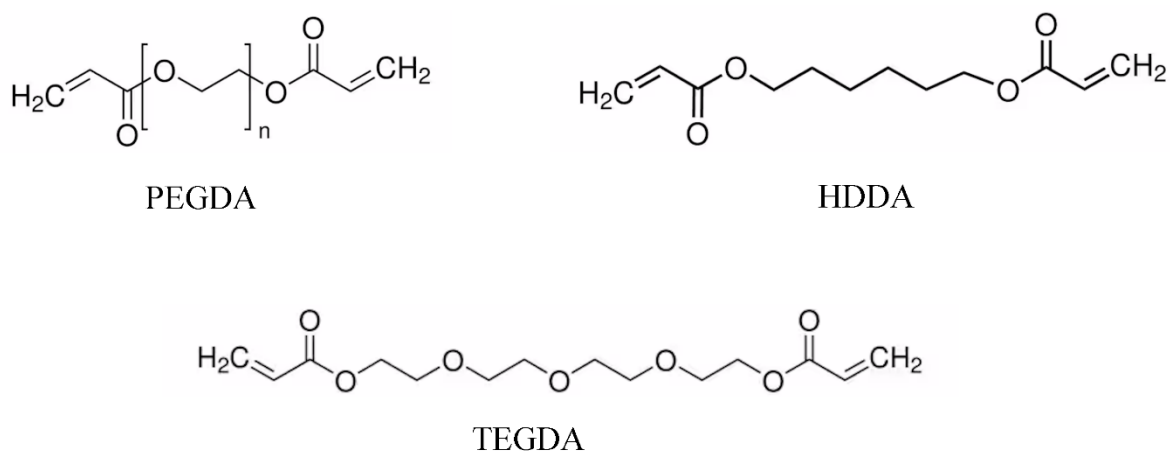


Figure 2.1: Chemical structures of the monomers investigated over the course of this work [49].

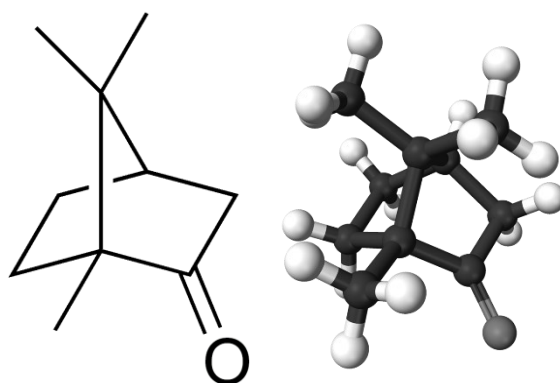


Figure 2.2: Chemical structure of Camphor (C₁₀H₁₆O) [50].

2.2. Preliminary analysis

The transmittance of the different monomers was measured with a V-570 spectrophotometer (JASCO) to find the one with the optical properties more suitable for VP.

Three resin formulations were prepared: HDDA/PEGDA250, HDDA/PEGDA575, HDDA/TEGDA, all with a 1:1 monomer weight ratio. The solubility of camphor in each composition was estimated by preparing mixtures with different camphor content. The considered resin/camphor ratios (in terms of weight) were 2, 1.7, 1.5 and 1.3 (corresponding to a camphor content of approximately 33 wt.%, 37 wt.%, 40 wt.% and 43 wt.% on the overall weight of the mixture). Camphor was dissolved in the resin with the help of a planetary mixer (ARE-250 CE, THINKY) and its solubility was evaluated by visual analysis of the transparency of the mixture.

2.3. Preparation of the ink

Several ink formulations were prepared to study the effect of different constituents on the properties of the ink. In particular, the parameters investigated were ceramic loading, amount of dispersant, type of monomer and presence of diluent (camphor). The ink formulations prepared in this study are reported in Table 2.2. Please note that the photoinitiator concentration was always 1 wt.% of the total monomer weight.

Table 2.2: Ink formulations prepared over the course of this work.

Solid loading [vol.% of the total ink]	Monomer ratio	Dispersant [wt.% of alumina weight]	Camphor [wt.% of the weight of the liquid fraction]
50 vol.%	HDDA	2 wt.%	35 wt.%
52 vol.%	HDDA	2 wt.%	35 wt.%
54 vol.%	HDDA	2 wt.%	35 wt.%
56 vol.%	HDDA	2 wt.%	35 wt.%
58 vol.%	HDDA	2 wt.%	35 wt.%
56 vol.%	HDDA	3 wt.%	35 wt.%
56 vol.%	HDDA	4 wt.%	35 wt.%
56 vol.%	HDDA/PEGDA575 1:1	2 wt.%	35 wt.%
56 vol.%	HDDA/PEGDA250 1:1	2 wt.%	35 wt.%
48 vol.%	HDDA/PEGDA250 1:1	2 wt.%	-
48 vol.%	HDDA/PEGDA250 1:1	2 wt.%	35 wt.%
56 vol.%	HDDA/PEGDA250 1:1	2 wt.%	-
56 vol.%	HDDA/PEGDA250 1:1	2 wt.%	35 wt.%

The liquid photocurable resin was prepared by mixing the monomers and dispersant, then camphor was progressively added to the formulation. To ensure its complete dissolution, each addition was followed by mixing in a planetary mixer (ARE-250 CE, THINKY) for 2 min at 2000 rpm. Once the mixture was homogenized, the alumina powder was gradually incorporated: a small amount of particles was poured into the resin and manually stirred in, then the suspension was put into the planetary mixer at 2000 rpm. Mixing time was usually 2 min, but could be increased up to 4 min in the case of particularly viscous formulations. These steps were repeated until all the ceramic particles had been added and were uniformly dispersed into the ink. A ball mill (Pulverisette 6 classic line, Fritsch) was then used to break down agglomerates formed by the particles and further homogenize the ink. Several ball milling parameters, including speed and duration, were varied to optimize the process. The speed of the ball milling was varied, but it could not exceed 350 rpm; otherwise, the ink would spill out of the jar.

After ball milling, the photoinitiator was added into the mixture, which was then homogenized by mixing in the planetary mixer at 2000 rpm for 2 min. At this point, the ink was ready and could undergo rheological characterization or be used directly for printing. To preserve it over time and prevent natural light from starting unwanted reactions, the container of the ink was wrapped in aluminum foil.

2.4. Printing

The printer utilized to fabricate the green bodies was a commercial SL1S SPEED (Prusa Research) with bottom-up configuration operating at a wavelength of 405 nm (Figure 2.3). This machine featured a 5.96" monochrome LCD with resolution 2560×1620 p.

The customizable printing parameters were:

- Layer thickness, which was set to 50 μm .
- “Layer exposure time”, which was the time for which a generic layer would be exposed to the UV light.
- “First layer exposure time”, which was the time for which the first printed layer would be exposed to the light. It was usually set to higher values than the previous parameter to ensure better adhesion between the green body and the building platform.
- The “setting” of the printer, which determined how fast the build head would move when it rose to detach the printer layer from the vat bottom and then descended again to prepare for

the new layer. For inks with higher ceramic loadings, it was necessary to change the setting from “Faster” to “Slower” and eventually “High viscosity” to achieve a successful and high quality print, but at the cost of longer printing time.

The optimal value of these parameters had to be determined for each ink composition and for each printed geometry.

With formulations based solely on HDDA, the build head was sometimes covered in a thin layer of PTFE-based grease prior to printing to make detachment of the printed objects easier.

After some preparatory experiments, two ink formulations with different solid loadings were chosen to fabricate the final samples: 48 vol.% and 56 vol.% alumina, both based on a resin composed of HDDA and PEGDA250 with a 1:1 monomer ratio, 2 wt.% dispersant and 35 wt.% camphor. Several geometries were considered, as shown in Figure 2.4. The final samples were printed in the shape of hollow cylinders with nominal external diameter 7 mm, height 7 mm and wall thickness 1.2 mm.



Figure 2.3: Commercial DLP printer Prusa SL1S SPEED.



Figure 2.4: Geometries that were printed during preliminary experiments. The final samples are in the shape of the hollow cylinder in the center of the image.

2.5. Post-processing

Once the printing was over, the samples were carefully detached from the build head with a razor blade and cleaned to remove the residual unpolymerized ink from the surface. After testing with several solvents it was decided to rinse the samples with water and scrub them with a toothbrush. Immediately after cleaning they were inserted in a UV-chamber (Robotfactory) for a post-curing operation.

The green bodies underwent thermal debinding and pre-sintering in a tubular furnace (Zetasinter, Zetamix by Nanoe) in argon (Ar) atmosphere. The heating rate was set to 1 °C/min (for 48 vol.% alumina) and 2 °C/min (for 56 vol.% alumina) until 1300 °C, then they were held in temperature for 1 h. The samples were then conventionally sintered at 1500 °C, 1550 °C and 1600 °C for 1h in air atmosphere at a heating rate of 10 °C/min in a high temperature muffle furnace (Nabertherm). The samples were naturally cooled to room temperature.

A typical temperature profile for conventional debinding and sintering is reported in Figure 2.5.

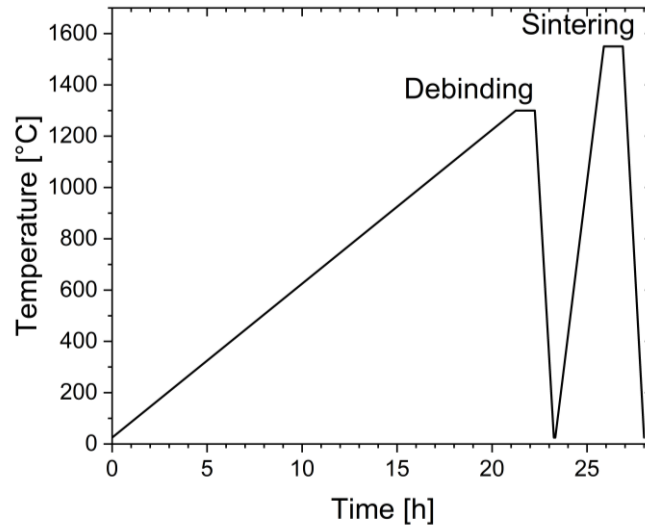


Figure 2.5: Temperature profile followed during debinding and conventional sintering of the prepared green samples.

Debinded samples fabricated with 56 vol.% alumina were sintered in Ar atmosphere with the UHS technology to verify the possible compatibility of UHS with AM. Each sample was sandwiched between two strips of 1 cm thick graphite felt (SGL carbon Co.) and fixed in contact with the metallic electrodes of a custom device (Figure 2.6) connected to an AC power supply (Item 3484, TECNA). This system worked at a fixed voltage of 7 V and current of 9 A, while the power varied, increasing as the felt heated and became more and more conductive, until a steady state was reached, usually in about 60 s (Figure 2.7). The higher the power, the higher the heat generated by the graphite felt. The average value of the power at the steady state was 240 W. The holding time was the other key parameter of the process and was set to 60 s, 300 s and 600 s respectively for different samples.

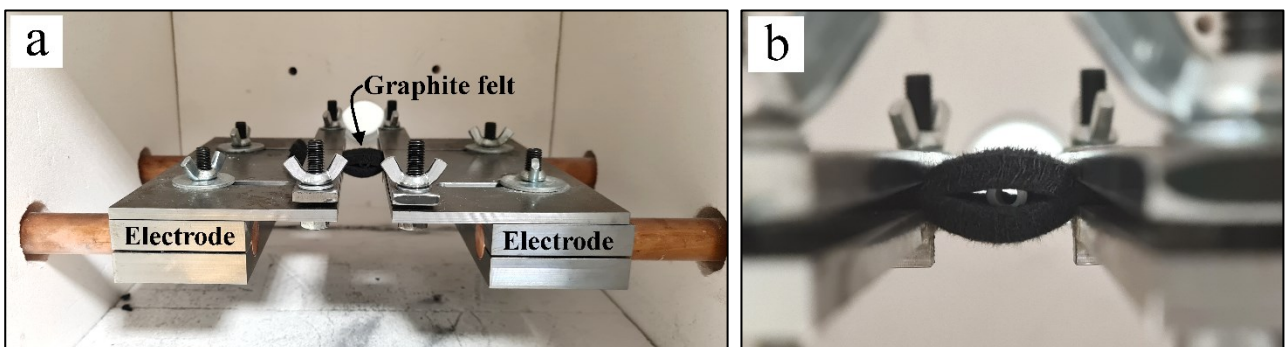


Figure 2.6: UHS configuration. a) Overview. b) Detail of a sample sandwiched between the carbon felt strips.

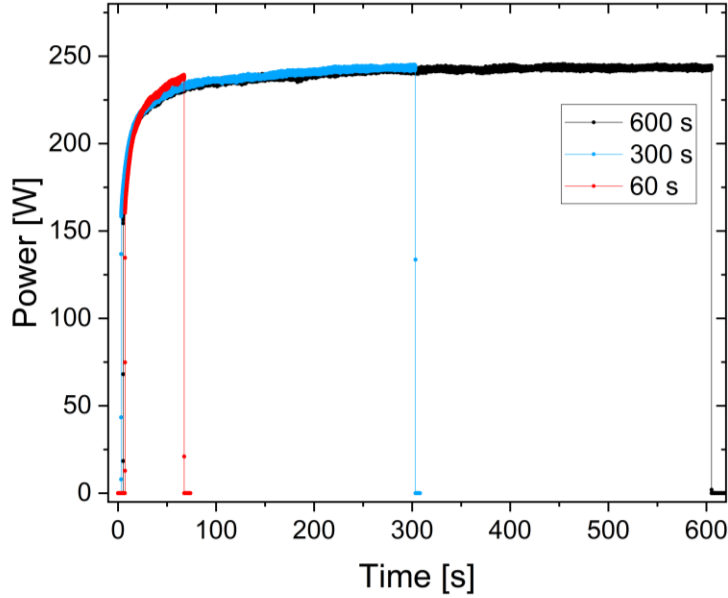


Figure 2.7: Power versus time curves of samples subjected to UHS for different holding times.

2.6. Characterization

A rotational rheometer (Kinexus prime lab+, Netzsch) with parallel plate configuration was used to characterize the inks in a range of shear rate comprised between 0.01 and 100 s⁻¹ at 25 °C. A plate with 40 mm diameter was used and the gap between plates was set to 0.5 mm. Shear stress vs shear rate curves as well as viscosity vs shear rate curves were obtained. The shear stress-shear rate curves detailing the effect of different solid loadings on the behavior of the suspension were fitted with the Herschel-Bulkley model.

Thermo-gravimetric analysis (TGA) of the printed samples and of camphor was carried out in Ar atmosphere with a heating rate of 10 °C/min (TGA/DSC 3+, Mettler Toledo).

Optical microscopy was performed to evaluate the presence of defects in the printed parts.

The dimensions of the samples were measured by means of a digital caliper with a sensitivity of 0.01 mm before debinding and after sintering to evaluate the linear shrinkage occurred.

The relative density (ρ) of the debinded and sintered parts was measured with Archimede's method using Equation 2:

$$\rho = \frac{\rho_b}{\rho_{Al_2O_3}} \cdot \frac{m_{dry}}{m_{wet} - m_b} \quad (2)$$

where ρ_b is the density of the buoyant medium (water at room temperature) that was approximated to 1 g/cm^3 , $\rho_{Al_2O_3}$ is the density of alumina, which was considered equal to 3.99 g/cm^3 [51], m_{dry} is the mass of the dry sample, m_{wet} is the mass of the sample measured after soaking it in water for 10 min in vacuum and m_b is the mass measured while the sample was immersed in water.

The phase composition of the alumina powders, of the samples sintered conventionally and of the samples consolidated through UHS was examined by X-ray diffraction (XRD) using a D8 ADVANCE diffractometer (Bruker) in the 2θ -range of $10\text{-}80^\circ$ ($\Delta(2\theta) = 0.02^\circ$ with a scan time of 1 sec/step) using $15 \text{ Cu K}\alpha$ radiation ($\lambda = 1.5418 \text{ \AA}$). The X-ray source operated at 40 kV and 40 mA.

External and fracture surface of the sintered parts were analyzed through scanning electron microscopy (SEM, Solaris, Tescan) after sputtering with 70 nm of chromium to obtain the microstructure and check the presence of defects.

Chapter 3

Results and discussion

3.1. Preliminary analysis

The ink must display high transmittance of light at the wavelengths at which the printer operates to obtain an adequate curing depth. The optical properties of the suspensions depend from those of the liquid medium. As can be seen from the transmittance curve in Figure 3.1, the monomer which shows the highest transmittance at a wavelength of 405 nm is HDDA, followed by PEGDA 575 and PEGDA 250 whose curves practically overlap in this region. TEGDA shows the worst optical properties out of all the monomers considered and was therefore excluded from the preparation of the samples.

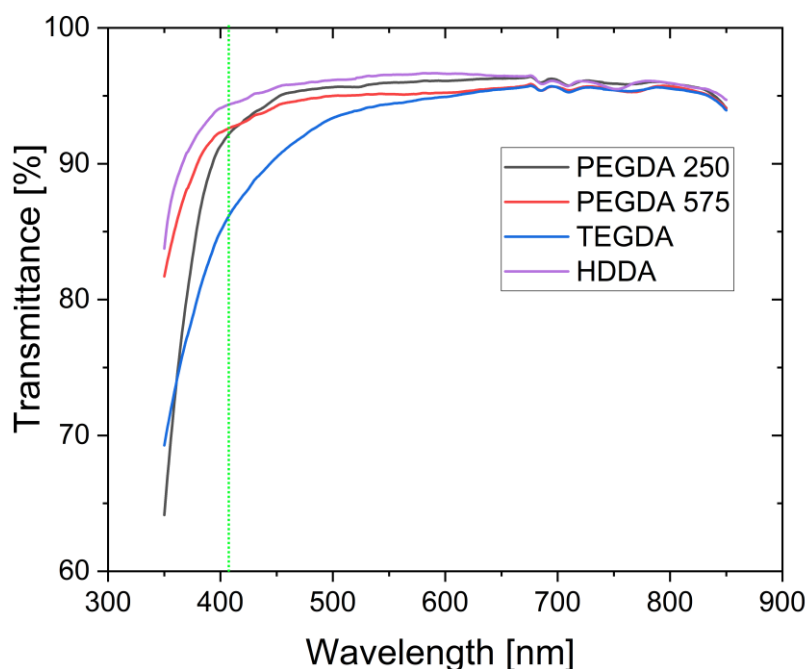


Figure 3.1: Transmittance curves of the monomers HDDA, TEGDA, PEGDA250 and PEGDA 575. The dotted green line represents the wavelength of 405 nm.

The solubility of camphor into different resin compositions was investigated to best exploit the positive effect of the diluent on the viscosity of the suspension. The optical appearance of the resulting

mixtures is reported in Table 3.1. The HDDA/PEGDA250 solution was the one that showed the highest solubility of camphor: it dissolved up to 40 wt.% on the weight of the mixture, while it remained undissolved at 43 wt.%, as can be observed in Figure 3.2. It was decided to keep the amount of diluent constant for all the prepared inks, both those based on HDDA only and those based on a HDDA/PEGDA250 mixture. Camphor content was fixed at 35 wt.% of the weight of the liquid fraction, to maintain a safety margin and always ensure complete dissolution.

Table 3.1: Visual appearance of the different mixtures for each resin/camphor ratio.

	Resin/camphor ratio (camphor wt.% on the total mixture weight)			
	2 (33 wt.%)	1.7 (37 wt.%)	1.5 (40 wt.%)	1.3 (43 wt.%)
HDDA/PEGDA250	Clear	Clear	Clear	Undissolved
HDDA/PEGDA575	Clear	Undissolved	Undissolved	-
HDDA/TEGDA	Clear	Clear	Undissolved	-

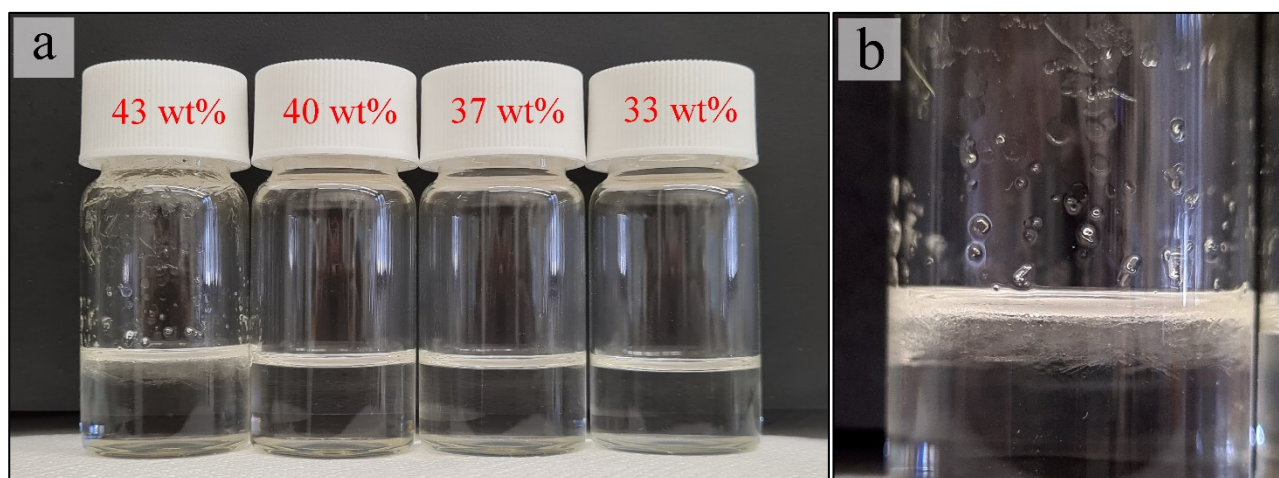


Figure 3.2: Mixtures prepared to evaluate the solubility of camphor in a HDDA/PEGDA250 resin with 1:1 monomer ratio. a) From left to right the resin/camphor ratio is 1.3, 1.5, 1.7, 2 respectively; the corresponding wt.% of camphor on the total weight of the mixture is reported on the cap of each container. b) Detail of undissolved camphor crystals for resin/camphor ratio equal to 1.3 (43 wt.% camphor).

3.2. Rheological characterization

3.2.1. Effect of the ceramic loading

The effect of solid loading on the rheological behavior was studied for HDDA-based inks with 2 wt.% dispersant, 35 wt.% camphor and solid loading of 50, 52, 54, 56 and 58 vol.% respectively. Inks were ball milled for 60 min at 300 rpm.

The viscosity-shear rate curves (Figure 3.3) show that all inks exhibit shear-thinning behavior: viscosity decreases when shear rate increases. This is an ideal characteristic for ceramic VP.

Increasing the solid loading causes an increase in viscosity at all shear rates. The only exception is observed at shear rates less than 0.1 s^{-1} for the composition with 54 vol.% alumina: in this region this ink exhibits lower viscosity than the composition with 52 vol.% and with 50 vol.% alumina. All inks satisfied the requirement of having a viscosity lower than $3 \text{ Pa}\cdot\text{s}$ at a shear rate of 30 s^{-1} except for the one with 58 vol.% alumina, therefore, the preferred solid loading chosen for this study was the highest possible one that satisfied this requirement, that is 56 vol.%.

Figure 3.4 reports the shear stress-shear rate curves fitted with the Herschel-Bulkley model. The values of the fitting parameters are reported in Table 3.2. The yield stress τ_0 and the consistency index k increased as the solid loading increased. This is consistent with what was expected, since a higher value of k corresponds to a higher viscosity of the suspension. In general, the value of n decreased as the solid loading of the ink increased. All suspensions showed $n < 1$, confirming the observation of shear thinning behavior, except for the 50 vol.% ink whose n was practically 1. This high value might be explained by the fact that the shear thinning behavior of this particular suspension is more evident at shear rates lower than 10 s^{-1} , while at shear rates between 10 and 100 s^{-1} the viscosity is almost constant and the behavior is closer to that of a Newtonian fluid. The ink with 52 vol.% alumina exhibits a similar plateau, while inks with higher solid loadings consistently display a shear thinning behavior in the whole range of shear rate considered. The R^2 of the Herschel-Bulkley model was higher than 0.999 for all ink formulations, indicating a high degree of fitting.

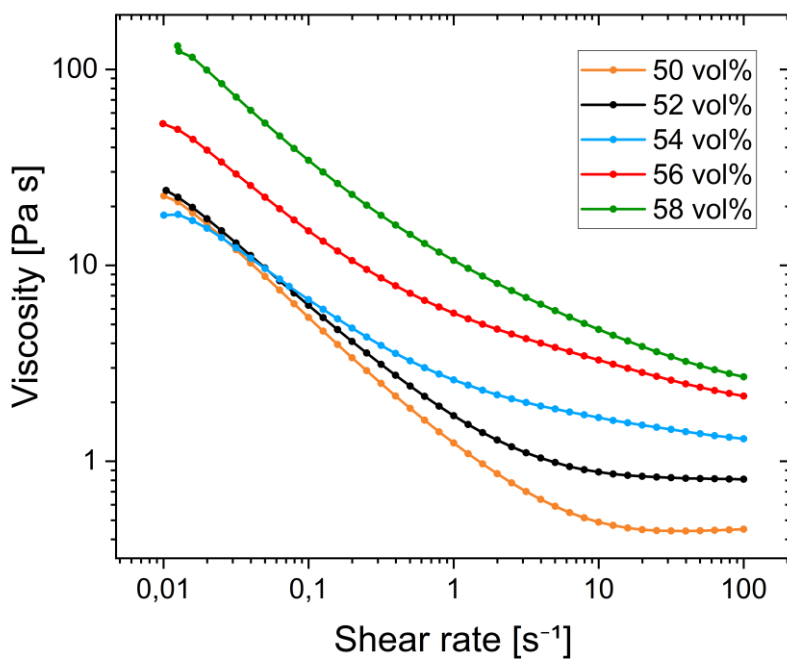


Figure 3.3: Viscosity versus shear rate curves detailing the effect of different solid loadings on the behavior of HDDA-based inks.

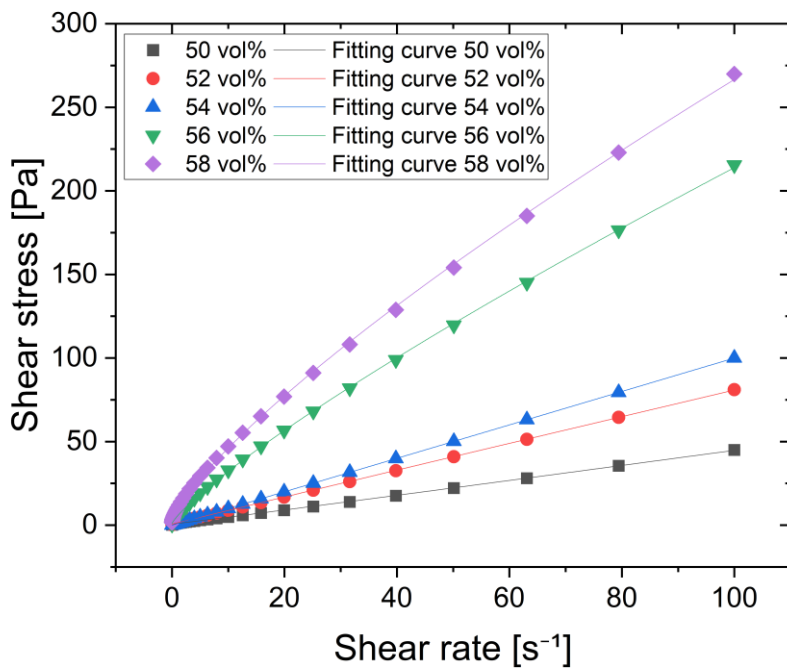


Figure 3.4: Shear stress-strain rate curves of HDDA-based inks with different solid loadings. The solid lines represent the fitting executed according to the Herschel-Bulkley model.

Table 3.2: Fitting parameters of the Herschel-Bulkley model for HDDA-based inks with different solid loadings.

Solid loading	τ_0	k	n	R^2
50 vol.%	0.62 ± 0.046	0.39 ± 0.127	1.007 ± 0.0074	0.99953
52 vol.%	0.63 ± 0.042	0.83 ± 0.012	0.993 ± 0.0035	0.99989
54 vol.%	0.76 ± 0.032	1.53 ± 0.031	0.865 ± 0.0018	0.99919
56 vol.%	1.0 ± 0.11	4.59 ± 0.055	0.833 ± 0.0028	0.99991
58 vol.%	2.7 ± 0.27	7.12 ± 0.151	0.784 ± 0.0048	0.99968

3.2.2. Effect of dispersant

The effect of the amount of dispersant on the rheology of the suspension was studied for HDDA-based inks with a solid loading of 56 vol.%, 35 wt.% camphor and dispersant amounts of 2, 3 and 4 wt.% of alumina weight respectively. Inks were ball milled for 60 min at 300 rpm. The rheological curves are shown in Figure 3.5.

It is evident that a higher amount of dispersant causes an increase in viscosity, likely due to increased interactions between the polymeric chains of the dispersant, which reduce the repulsion force between ceramic particles. The ink with 2 wt.% dispersant was the one with lowest viscosity and the only one that satisfied the requirement of viscosity lower than 3 Pa·s at a shear rate of 30 s⁻¹. For this reason, 2 wt.% was chosen as the optimized amount of dispersant to be used for the preparation of the final samples.

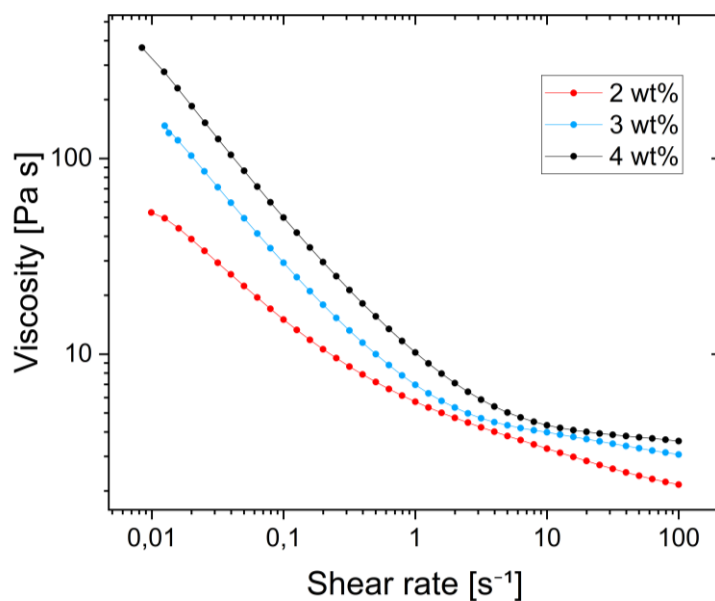


Figure 3.5: Viscosity versus shear rate curves detailing the effect of different amounts of dispersant on the behavior of HDDA-based inks with 56 vol.% solid loading.

3.2.3. Effect of the monomer

While HDDA showed the best optical properties and a sufficiently low viscosity, it was found that samples printed from HDDA-based compositions were very difficult to detach from the building platform of the printer. Significant force needed to be applied and this often resulted in damage to the samples, which consequently were unfit for further experiments. To solve this problem, different resins compositions were investigated. TEGDA was excluded due to its unfavorable optical properties. HDDA/PEGDA250 and HDDA/PEGDA575-based inks, both with 1:1 monomer ratio, 56 vol.% alumina, 2 wt.% dispersant (on alumina weight) and 35 wt.% camphor (on the weight of the liquid fraction) were prepared. They were ball milled for 120 min at 350 rpm. In Figure 3.6 their rheological behavior is compared to that of an HDDA-based ink with 56 vol.% alumina, 2 wt.% dispersant and 35 wt.% camphor. The HDDA-based ink shows the lowest viscosity, but the other two inks still have sufficiently low viscosity to be suitable for VP. Both PEGDA250 and PEGDA575 proved effective in facilitating detachment of the printed samples from the building platform. The ink based on the HDDA/PEGDA250 mixture had lower viscosity, therefore this composition was chosen for further experiments.

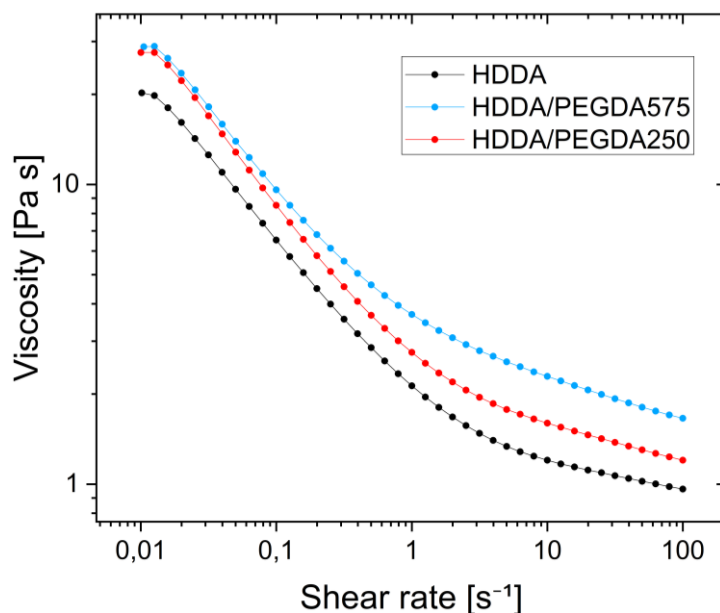


Figure 3.6: Viscosity versus shear rate curves of inks with 56 vol.% alumina based on different monomer mixtures.

3.2.4. Effect of camphor

The efficacy of camphor was verified by comparing the rheological behavior of two pairs of HDDA/PEGDA250-based formulations with 2 wt.% dispersant, ballmilled for 120 min at 350 rpm:

- Solid loading of 48 vol.%, without camphor and with 35 wt.% camphor (on the weight of the liquid fraction) respectively;
- Solid loading of 56 vol.%, without camphor and with 35 wt.% camphor (on the weight of the liquid fraction) respectively.

It is possible to notice in the viscosity versus shear rate curves in Figure 3.7 that the inks with camphor show much lower viscosities than their camphor-less counterparts. The diluent effect is particularly evident in the inks with 56 vol% alumina: the one with no camphor does not satisfy the requirement of viscosity lower than 3 Pa·s at a shear rate of 30 s⁻¹ while the ink with camphor does.

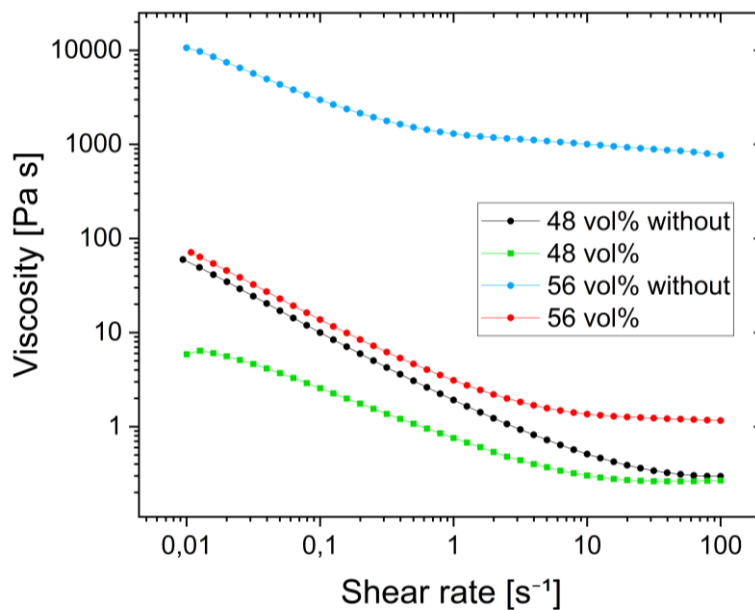


Figure 3.7: Viscosity versus shear rate curves of 48 vol.% and 56 vol.% HDDA/PEGDA250-based inks, with and without camphor in the formulation, showing the effect of the diluent.

3.2.5. Effect of the ball milling time

Ball milling the ink is useful to break down aggregates formed by the ceramic particles and to homogenize the suspension, improving the rheological behavior and preventing the formation of concentration gradients in the printed bodies.

The optimal ball milling time was determined by comparing the rheological curves (Figure 3.8) of a HDDA-based ink with 56 vol.% solid loading, 2 wt.% dispersant and 35 wt.% camphor milled at 350 rpm for different times. All curves exhibit shear thinning behavior and viscosities lower than 3 Pa·s at a shear rate of 30 s^{-1} , thus displaying suitable behavior for VP.

It was observed that increasing the ball milling time between 30 min and 120 min generally caused a decrease in viscosity, especially at low shear rates. The ink milled for 30 min consistently shows the highest viscosity, while for shear rates between 10 and 100 s^{-1} a ball milling time of 60 min results in the lowest viscosity. At very high shear rates (around 100 s^{-1}) instead there seems to be no significant difference between the behavior at 60, 90 and 120 min.

The curve obtained for a ball milling time of 180 min overlaps with the 120 min one at shear rates smaller than 10 s^{-1} , then they diverge slightly with the ink milled for 180 min exhibiting slightly lower viscosities at very high shear rates. The curve obtained for 240 min breaks the trend observed so far: this ink always displays considerably higher viscosity than the ink milled for 180 min. It is possible to conclude that ball milling beyond 120 min brings no significant improvement and actually worsens the rheological behavior of the ink when the time approaches 240 min. This is related to the onset of a new phenomenon: until 180 min the primary effect of milling is to break down the aggregates of particles; when all aggregates have been eliminated, it is the particles themselves that start to be broken into smaller pieces, and powders of smaller size result in inks of higher viscosity.

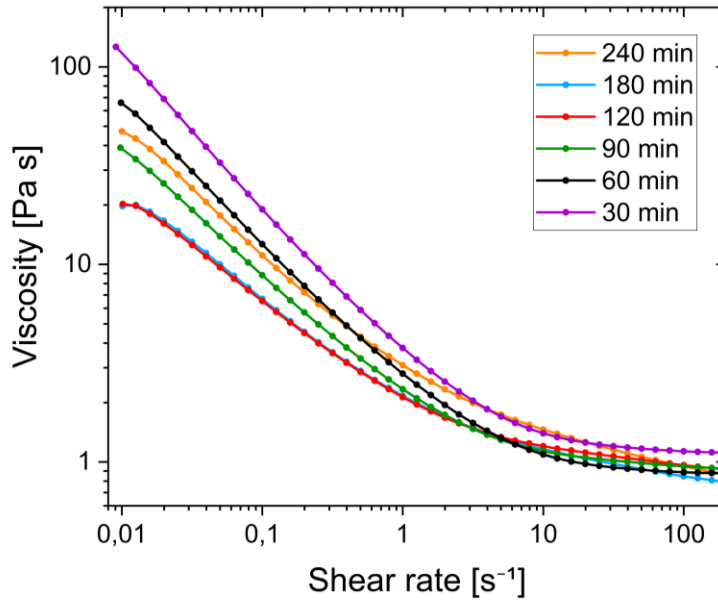


Figure 3.8: Viscosity versus shear rate curves of 56 vol.% HDDA-based inks displaying the effect of the ball milling time on the rheological behavior.

3.3. Printing

The printing parameters had to be optimized for each composition and geometry. In general, it was observed that:

- As expected, there is a minimum “layer exposure time” that is necessary to ensure complete curing of a layer. Slight increases of the curing time beyond this value do not seem to provide significant improvements, while a much larger “layer exposure time” caused overcuring and evident loss of dimensional accuracy, as well as longer printing time.
- Increasing the “first layer exposure time” led to a stronger adherence between the printed samples and the building platform, thus decreasing the risk of the layers detaching and increasing the likelihood of the print being successful, but at the cost of a longer printing time.
- Inks with 56 vol.% solid loading could only be printed with the setting “High viscosity”. Inks with sufficiently low viscosity (i.e. less than 50 vol.% alumina) could be printed setting the machine to “slower”, significantly shortening the duration of the printing operation.
- Structures with small wall thickness (<1 mm) tended to stick to the bottom of the vat more than to the building platform. The addition of a base pad with the slicing software allowed to increase adherence to the head and resulted in more successful prints. Increasing the “first layer exposure

time” and “layer exposure time” also increased the chances of the print being successful, likely because the structure was overcured and the contact area between different layers increased.

- The amount of ink present in the vat also influenced the outcome of the print: higher ink volumes often resulted in less successful prints. This might be due to the forces exerted by the flowing ink on the samples when the building platform rose and descended again in between curing the layers.

3.4. Thermogravimetric analysis

TGA was performed to study the thermal decomposition behavior of camphor and of the green bodies with 48 vol.% and 56 vol.% alumina (Figure 3.9). The initial mass loss until 200 °C is attributed to the sublimation of the camphor (Figure 3.9(b)). The most intense mass loss happens between 350 – 500 °C with the highest mass loss rate observed at around 420 °C for both the compositions. With increasing temperature and beyond 500°C mass loss approached zero, denoting that the organic fraction has almost completely decomposed. As expected, the residual mass measured for the 56 vol.% samples at the end of the process is higher than the mass measured for the 48 vol.%: 85.5 wt.% versus 83.4 wt.%. Both of these values are higher than the initial alumina content of the ink (83.8 wt.% for the 56 vol.% and 78.3 wt.% for the 48 vol.%), which indicates that some residues from the organic decomposition were still left due to incomplete combustion as the analysis was carried out in inert atmosphere. It might also happen that some of the camphor might evaporate during the ball milling process because of the heat generated by the impact of the balls used for milling.

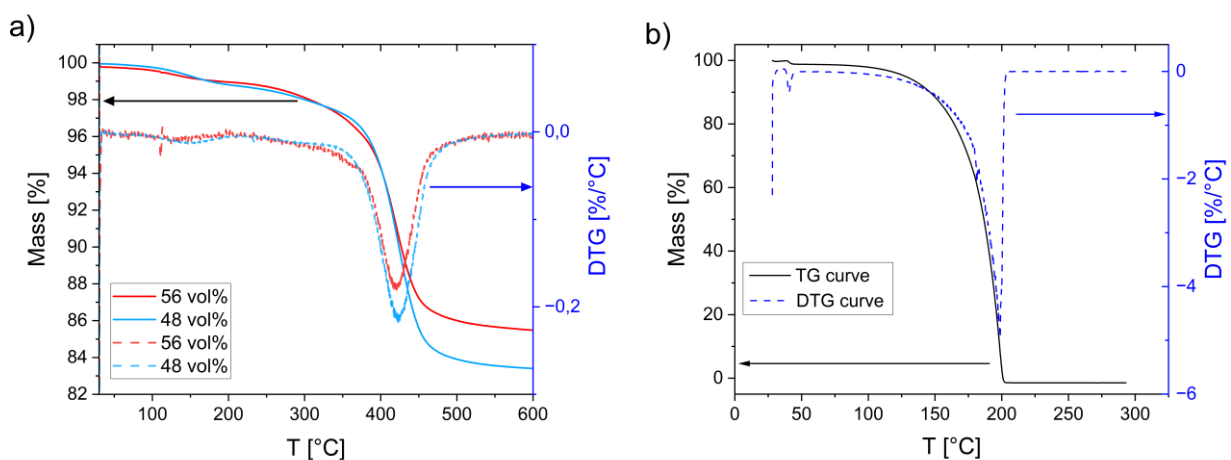


Figure 3.9: a) *TG and DTG curves of the green bodies with 48 vol.% and 56 vol.% alumina. The solid line represents the TG curve and the dashed line the DTG curve.* b) *Result of the thermal decomposition of camphor.*

3.5. Post processing

3.5.1. Cleaning solvent

Different solvents were tested to estimate their effectiveness at removing residual ink from the printed bodies. Ethanol, isopropanol, acetone, propylene carbonate and 2-phenoxyethanol were found to be too aggressive and led to the formation of delaminations on the samples. This was due to the high solubility of camphor in these solvents (as confirmed by dissolving camphor in these solvents). Water was not very effective by itself but its efficacy was improved with the use of a toothbrush, which mechanically removed the residual resin from the surface of the printed samples without any major delamination.

3.5.2. Post-curing time

Even when cleaning with an appropriately non-aggressive solvent, the samples tended to delaminate over the course of time, therefore the effectiveness of a post-curing operation was investigated. Samples were cured for 2, 4, 5, 7, and 10 minutes respectively and then they were analyzed with an optical microscope to evaluate the presence of defects. A curing time of 2 min was insufficient because the samples still exhibited delaminations. Samples cured for 4 and 5 min showed no defects, while samples cured for 7 and 10 min showed some delaminations, probably due to overcuring. For these reasons, post-curing for 4 min was deemed necessary to reduce the amount of defects developed by the printed samples.

In Figure 3.10 it is possible to compare the appearance of a sample that was not post-cured after being removed from the printer with that of a sample that was subjected to post-curing for 4 min. The former presents evident delaminations and is unsuitable for further thermal treatments. Starting from a green body with so many delaminations would result in a final ceramic body of low quality. Conversely, the sample that has been post-cured shows no macroscopic defects and is a good starting point for the production of a dense ceramic object.

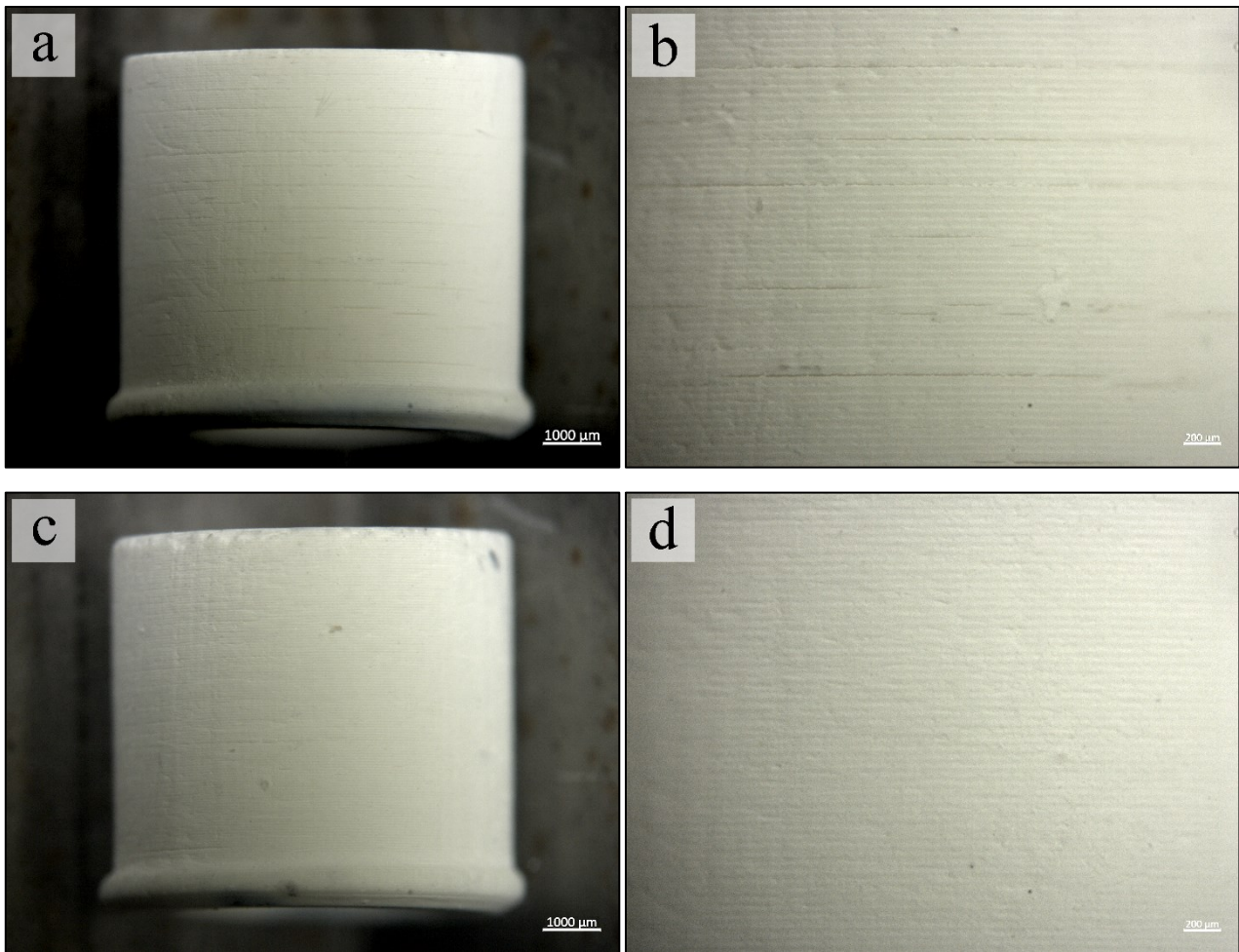


Figure 3.10: Comparison between a not post-cured sample (a, b) and a sample that was subjected to 4 min of post-curing (c, d). The sample that was not post-cured shows evident delaminations while the post-cured sample appears free of defects.

SEM micrographs (Figure 3.11) of some of the fracture surfaces revealed that delaminations were not completely eliminated even in the post cured samples, but they were significantly reduced in dimensions. Interestingly, in both types of samples the delaminations were only present on the external surface of the body, while the core showed good interlayer bonding. Based on these observations, we can hypothesize that the defects are generated either during cleaning, perhaps due to a still too aggressive removal of the unpolymerized resin from the surface, or even during printing. The lateral border of a layer tends to suffer the most from light scattering, especially at high solid loading. Radiation scattered sideways has a reduced energy that, while sometimes sufficient to initiate the photopolymerization reaction, might be too low to guarantee an adequate curing depth throughout the whole layer thickness [19]. This could result in poor interlayer bonding and consequent delamination at the border of the layers, which corresponds to the external surface of the sample.

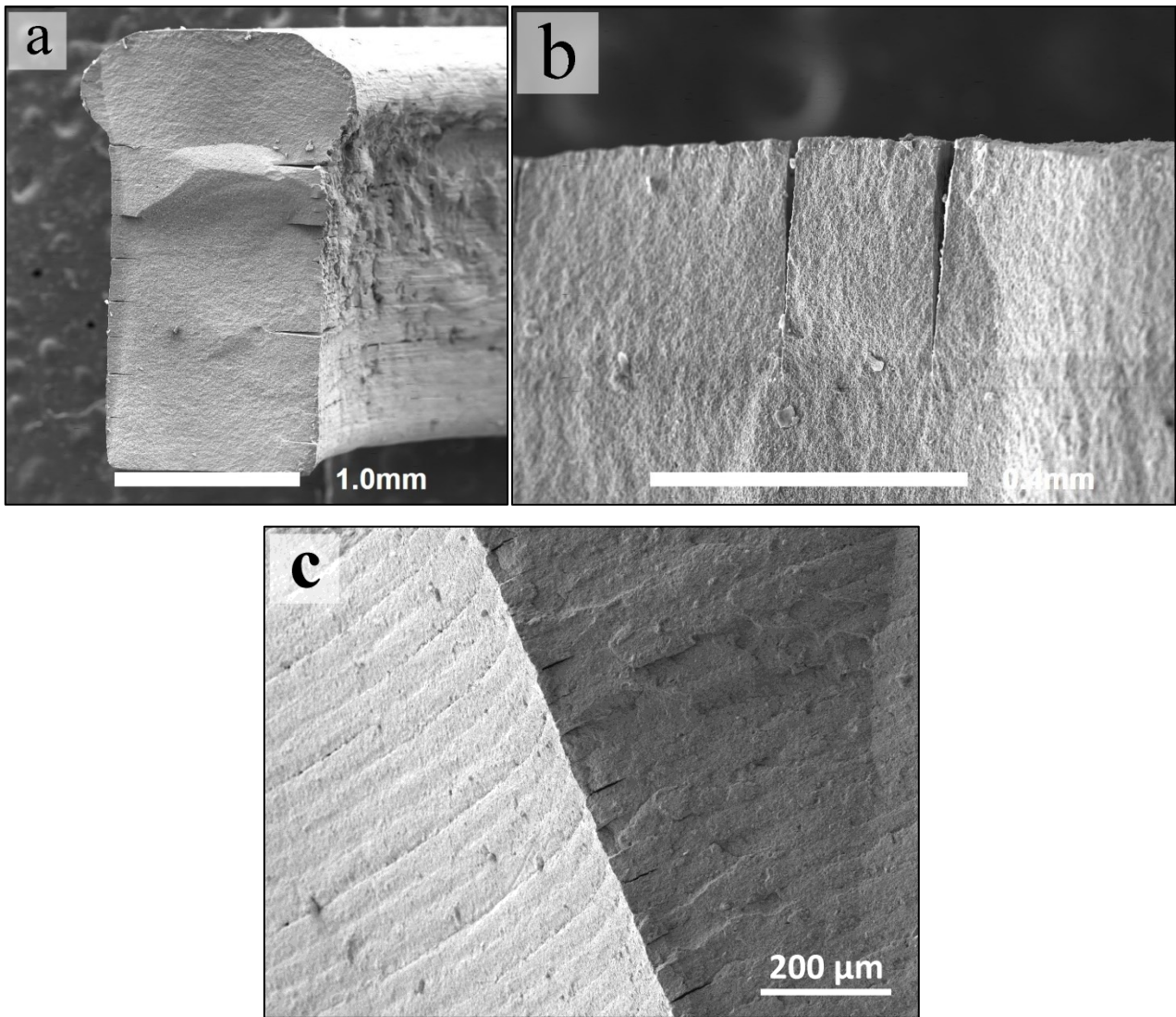


Figure 3.11: SEM micrographs of the fracture surfaces of a sample that was not post-cured (a, b) and of a post-cured sample (c). Delaminations are much more severe when post-curing has not been performed.

3.6. Debinding and sintering

3.6.1. Shrinkage

Figure 3.12 and Figure 3.13 depict the optical appearance of the sintered samples with two different ceramic loadings (48 vol.% and 56 vol.% respectively). It is quite evident that samples of both compositions underwent a significant reduction in volume during the thermal treatments. It is also interesting to note that shrinkage was higher for the samples with 48 vol.% alumina when compared to the one with 56 vol.% as evident in Figure 3.14.

The linear shrinkage along the building direction (along the axis of the cylindrical sample) and the radial direction (in the plane of the layers, that is along the diameter of the cylinder) after sintering has been depicted in image (a) of Figure 3.16. One can observe that for a given composition and sintering temperature the axial shrinkage was always higher than the radial shrinkage. This anisotropy is caused by the layer-by-layer approach, typical of AM processes. In addition, the shrinkage also increases with the sintering temperature, which is in good agreement with the density and microstructural analysis detailed later on.

A very similar shrinkage trend was observed for the UHS: shrinkage increases with the holding time (image (b) of Figure 3.16). The shrinkage of the UHSed samples was comparable to that of the ones sintered conventionally. For instance, the shrinkage of the sample subjected to UHS for 600 s is equal to 21.4% in the axial direction and 16.4% in the radial direction, very close to the 22.0% in the axial direction and 16.8% in the radial direction of the samples sintered conventionally at 1600 °C.

The shrinkage undergone by the UHS samples is also evident from their visual appearance, depicted in Figure 3.15. It can also be observed that the color of the sintered ceramic parts gets increasingly darker as the holding time used for UHS gets longer. This change of color might be caused by carbon contaminations coming from the felt or due to reduction of the oxide when sintered in inert atmospheres with low $P(O_2)$.

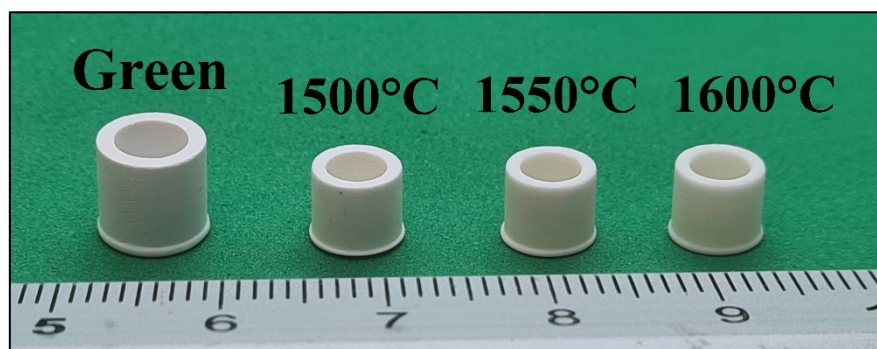


Figure 3.12: Comparison between the green and the sintered samples prepared from the HDDA/PEGDA250-based ink with 48 vol.% alumina. Sintering temperatures are indicated in the image.

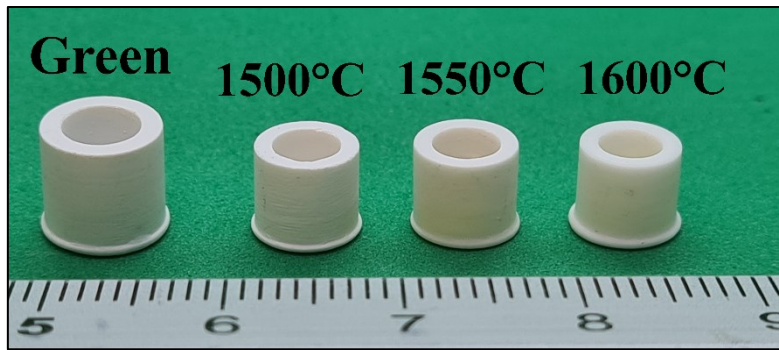


Figure 3.13: Comparison between the green and the sintered samples prepared from the HDDA/PEGDA250-based ink with 56 vol.% alumina. Sintering temperatures are indicated in the image.

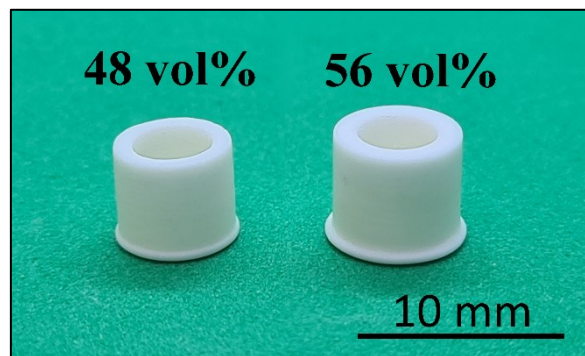


Figure 3.14: Visual comparison of two samples sintered at the same temperature (1600 °C) but prepared from inks with different solid loadings, as indicated in the image.

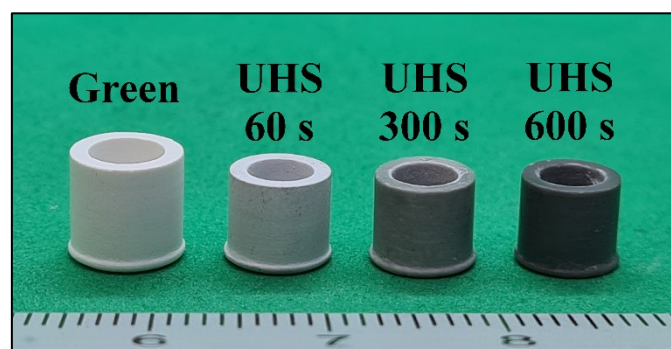


Figure 3.15: Comparison between samples prepared from the HDDA/PEGDA250-based ink with 56 vol.% alumina, green and subjected to UHS. Holding times are indicated in the image.

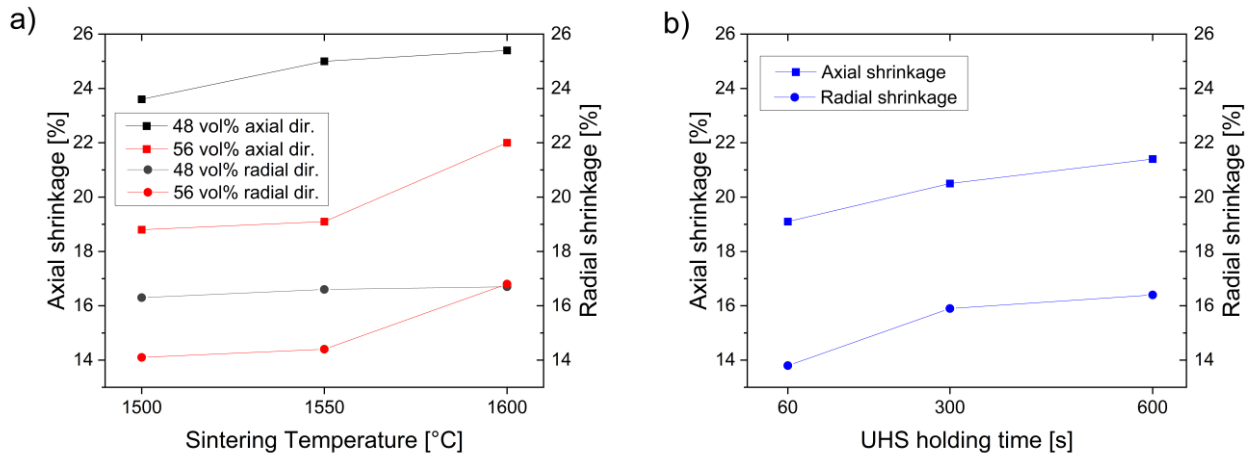


Figure 3.16: Linear shrinkage in the building direction and in the radial direction of the samples subjected to different thermal treatments. a) Samples sintered conventionally at different temperatures. b) Samples subjected to UHS for different holding times.

3.6.2. Density

The debinded samples had a low relative density. Those derived from the ink with 56 vol.% alumina had an average relative density (69.2%) higher than that of the samples prepared from the ink with 48 vol.% solid loading (58.2%). Therefore, lower solid loadings result in more porous structures after the removal of the binder.

The relative density of the conventionally sintered and UHSed samples has been shown in Figure 3.17. The samples subjected to conventional sintering exhibited densities greater than 95% except for the 48 vol.% samples sintered at 1500°C, whose average relative density was 92.8%. It was observed that a slightly higher relative density could be achieved by increasing the sintering temperature or by starting from an ink with higher solid loading. The relative densities of the samples sintered at 1600°C were almost the same (average of 96.8% for the 48 vol.% samples and 96.4% for the 56 vol.% samples), suggesting that this temperature is sufficient to remove most of the open porosities.

The sample subjected to UHS for 60 s resulted in a low relative density (84.9%), confirming that this holding time is inadequate to densify the debinded sample. Samples held for 300 s and 600 s achieved good relative densities (96.9% and 98.0% respectively), slightly higher than those obtained for the samples sintered through conventional method.

Overall, an optimized UHS process seems to be able of producing ceramic samples of comparable quality of those obtained through conventional sintering. This is a very promising result, because

UHS significantly shortens the time required to manufacture an object and could lead to more time- and energy-efficient production processes.

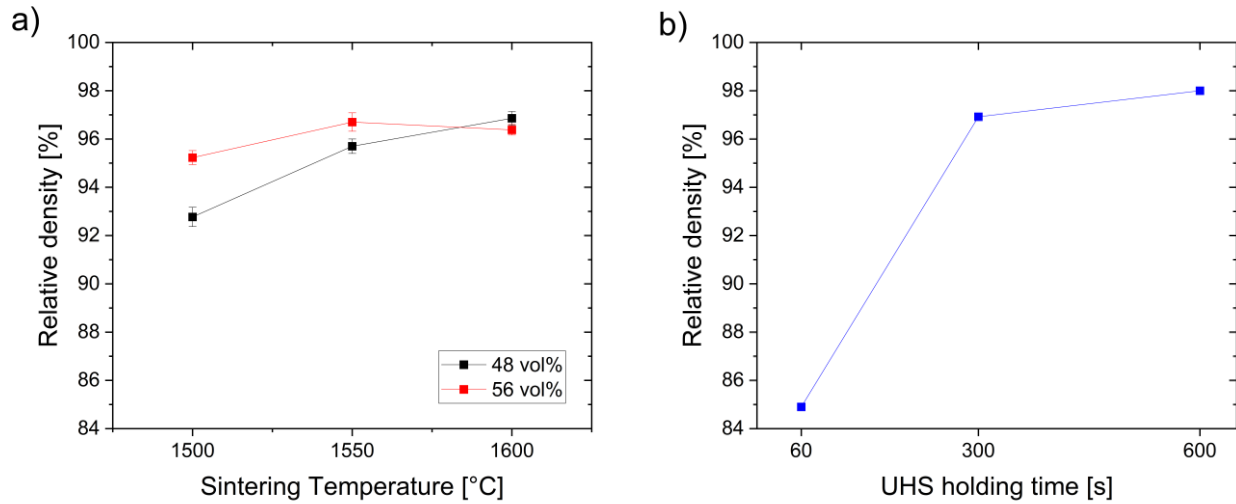


Figure 3.17: Average relative density of samples subjected to different thermal treatments. a) Samples sintered conventionally at different temperatures. b) Samples subjected to UHS for different holding times.

3.6.3. X-ray diffraction

The XRD patterns of the alumina powders, the samples sintered conventionally at 1500 °C and 1550 °C and the samples subjected to UHS for 60 s and 300 s are shown in Figure 3.18. The peaks highlighted by black diamonds are located at 25.6°, 35.1°, 37.8°, 43.4°, 52.6°, 57.5°, 59.8°, 61.2°, 66.5° and 68.2° and correspond to the (012), (104), (110), (113), (024), (116), (211), (018), (214) and (300) crystallographic planes of α -Al₂O₃ [12], [52], [53], [54]. This confirms that all the obtained samples consisted of a single phase of α -alumina and no evidence of any new phase could be observed.

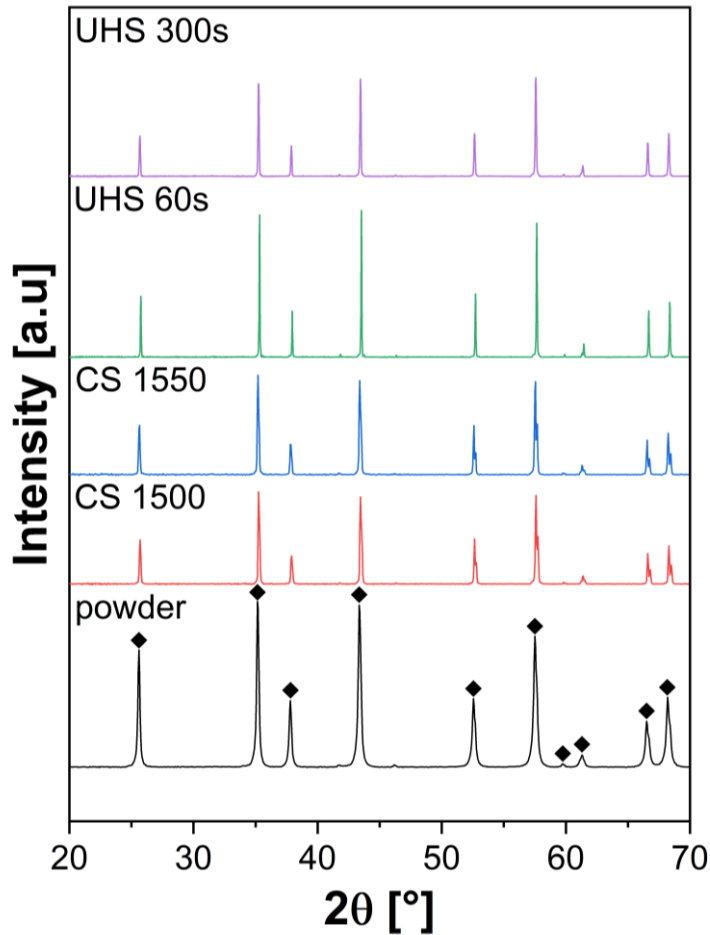


Figure 3.18: XRD patterns of the alumina powder, samples sintered conventionally at 1500 °C and 1550 °C, and samples subjected to UHS for 60 s and 300 s. The black diamonds point out the major peaks.

3.6.4. SEM of debinded samples

The micrographs of the debinded samples observed through SEM (Figure 3.19) reveal a porous microstructure consisting of fine, loosely connected particles. The particle size that can be estimated from the images is coherent with the median particle size of 0.5 μm of the starting alumina powders, however some particles with bigger dimensions were found to be randomly distributed in the structure. Samples fabricated with 56 vol.% alumina appear slightly less porous than those obtained from inks with 48 vol.% solid loading, coherently with the observations made from measuring their relative density. No other significant difference can be observed at this stage between samples obtained from inks of different compositions.

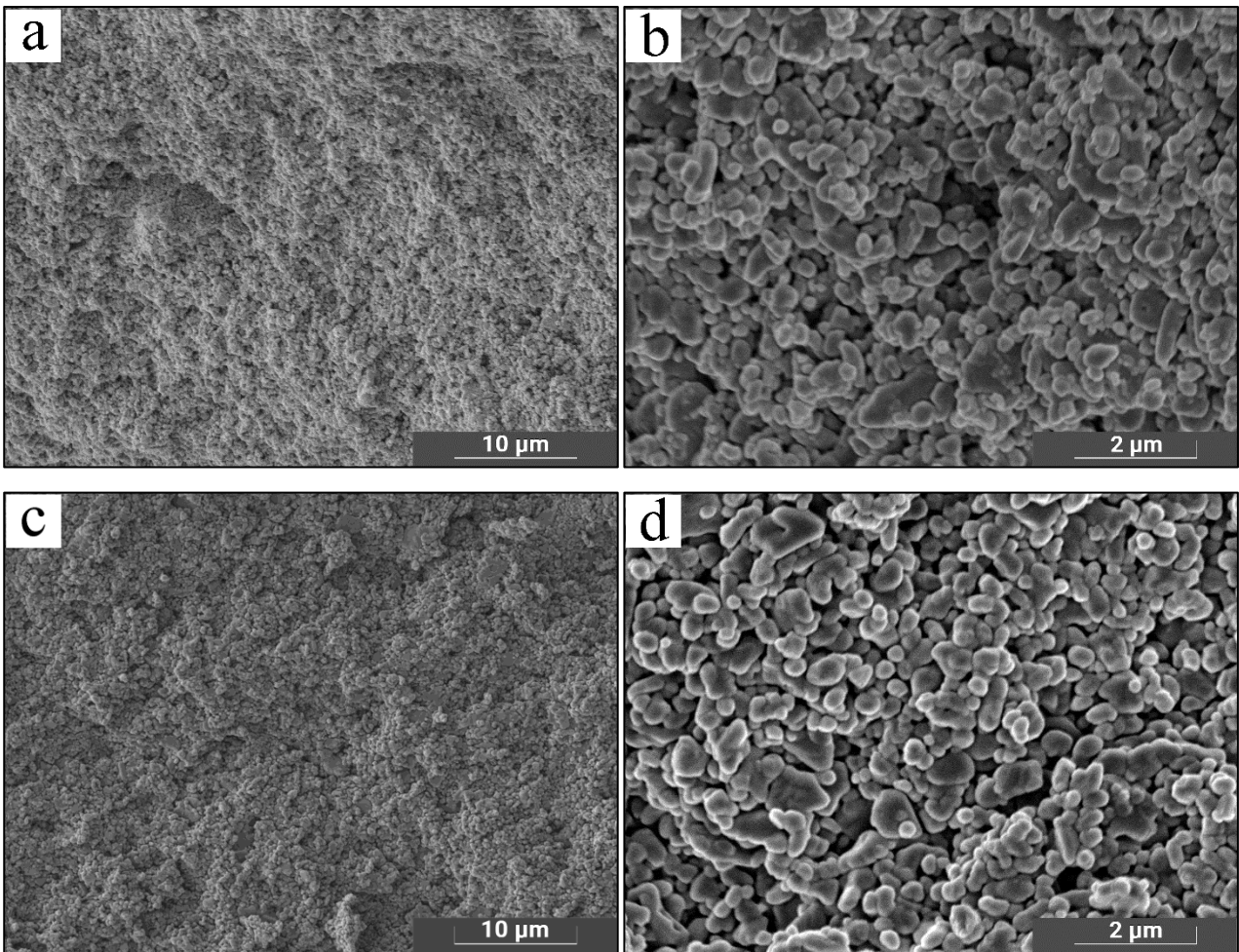


Figure 3.19: SEM micrographs of the fracture surfaces of debinded samples derived from inks with solid loading 48 vol.% (a, b) and 56 vol.% (c, d) respectively.

3.6.5. SEM of the conventionally sintered samples

The microstructure of the sintered samples from inks with 48 vol.% alumina is shown in Figure 3.20 and that of samples with 56 vol.% alumina is reported in Figure 3.21. At 1500 °C, the microstructure is quite fine, however, some isolated porosity can be still observed at the junction of the grain boundaries. With increase in temperature, the porosity decreases and grain growth occurs. One can also notice the change in fracture mechanism from intergranular to transgranular with increase in the sintering temperature or grain size. In a fine microstructure, the grain boundary area is significantly larger, making grain boundaries more prone to crack propagation, especially considering the potential presence of pores at triple points. On the other hand, in a coarse microstructure with fewer grain boundaries, the likelihood of a crack being deflected along a grain boundary is reduced, leading to propagation through the grains instead [55].

The microstructures of samples with different solid loadings treated at the same temperature were also compared. For sintering temperatures of 1500 °C and 1550 °C, the samples from inks with 48 vol.% alumina appear more porous than the corresponding samples from inks with 56 vol.% alumina. This can be noticed especially in Figure 3.20 and Figure 3.21 in images (b) and (c) for 1500 °C and images (e) and (f) for 1550 °C. There was instead no noticeable difference in porosity for samples of different compositions sintered at 1600 °C as consistent with the density measurement in Figure 3.17.

Overall, the microstructures were quite homogeneous, however, the 56 vol.% samples exhibited some local inhomogeneities in grain size and density. This phenomenon is particularly noticeable in image (b) and (h) of Figure 3.21 (marked in yellow circle) and might be caused by inhomogeneities present in the original green body. The elevated viscosity of a suspension with high solid loading makes it more difficult to uniformly distribute the particles through the resin. It is possible that local inhomogeneities formed while the ink was stored or during the printing operation, then they were fixed in place during photopolymerization and the thermal treatments could not completely remove them. The hypothesis that high ink viscosity is the root cause of these local inhomogeneities is also supported by their absence in samples prepared from inks with 48 vol.% solid loading, which had a considerably lower viscosity and could be mixed much more easily.

Images of the external surface of the sintered samples acquired through SEM are shown in Figure 3.22. No delaminations could be detected and a good interlayer bonding has been achieved for both 48 vol.% and 56 vol.% samples. Some printing defects and open porosities are present, like those visible in image (b) of Figure 3.22, but the overall surface quality is good. All samples clearly display the “staircase effect” typical of AM products built layer-by-layer. Nonetheless, the dimensions of the ridges and valleys is of the order of 10 μm, resulting in excellent surface finish.

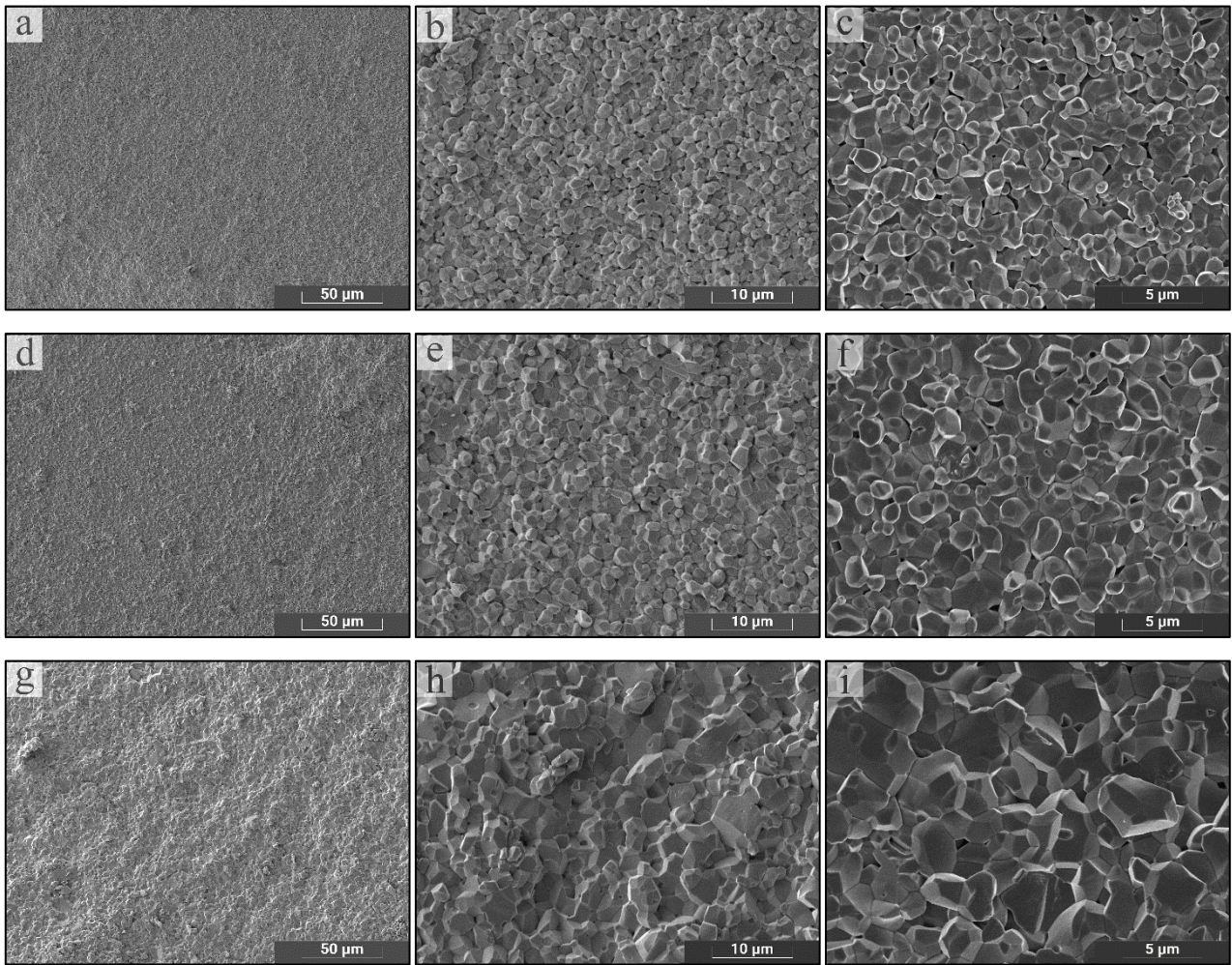


Figure 3.20: SEM micrographs showing the effect of the sintering temperature on the microstructure of samples produced from the HDDA/PEGDA250-based ink with 48 vol.% alumina. The samples were conventionally sintered for 1 h at different temperatures: 1500 °C (a, b, c), 1550 °C (d, e, f) and 1600 °C (g, h, i).

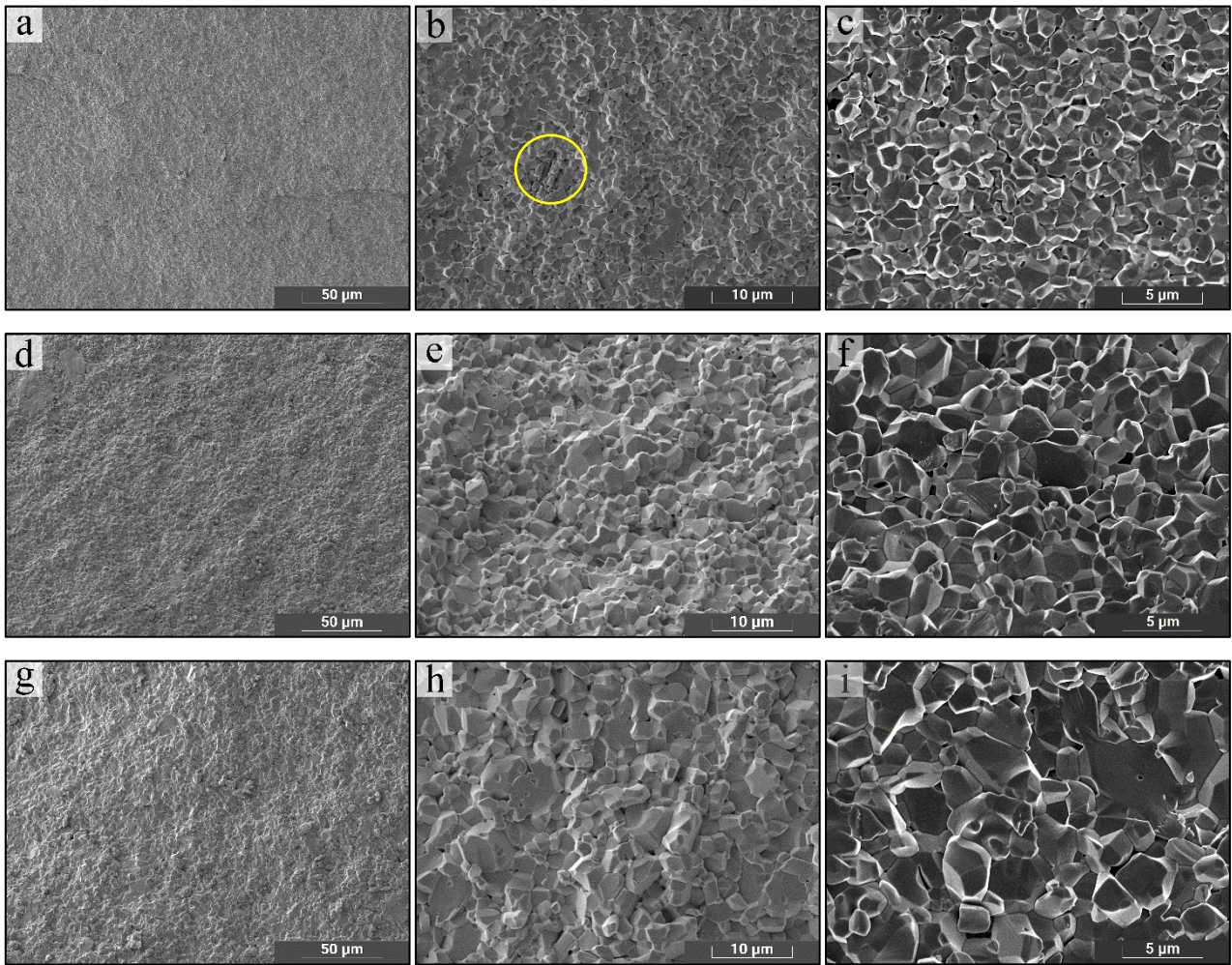


Figure 3.21: SEM micrographs showing the effect of the sintering temperature on the microstructure of samples produced from the HDDA/PEGDA250-based ink with 56 vol.% alumina. The samples were conventionally sintered for 1h at different temperatures: 1500 °C (a, b, c), 1550 °C (d, e, f) and 1600 °C (g, h, i).

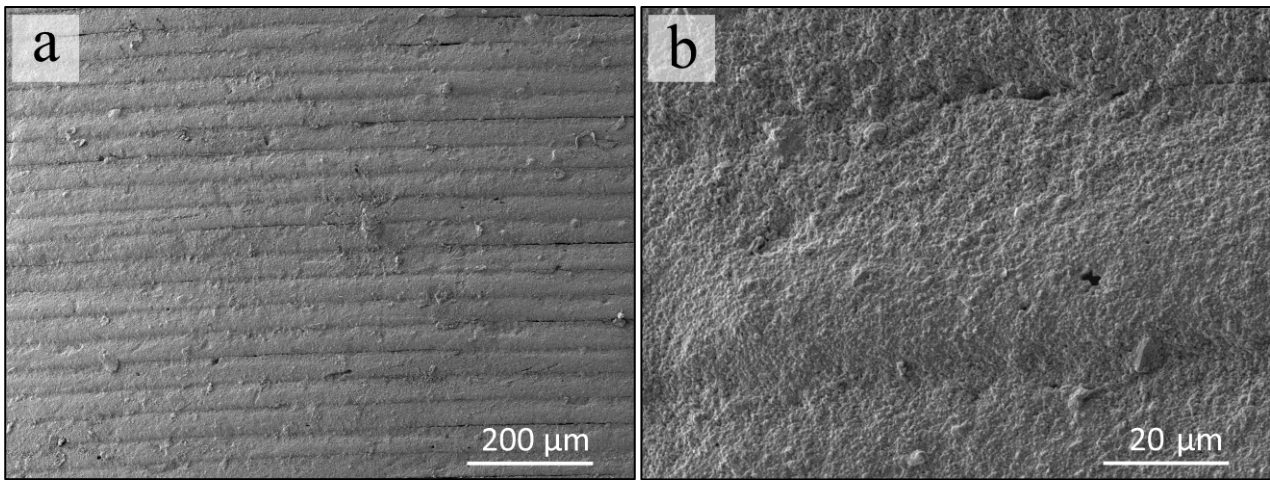


Figure 3.22: Typical external surface of the samples sintered through conventional methods. a) Overview showcasing the staircase effect. b) Detail with an open porosity clearly visible in the right side of the image.

3.6.6. SEM of UHS samples

Micrographs of the fracture surfaces of the UHS samples were acquired through SEM to analyze the effect of different holding times on the microstructure (Figure 3.23). It was determined that longer holding times lead to a bigger average grain size. The sample subjected to UHS for 60 s had an extremely fine microstructure, with grain size very close to the dimensions of the alumina powder, but displayed a considerable amount of porosities. With increasing power (which means increasing temperature), the porosity disappeared and the samples exhibited coarser grains. For example, the sample held for 300 s had a grain size and level of porosity comparable to that of the samples with the same composition that underwent conventional sintering at 1500 °C. The sample subjected to UHS for 600 s instead had a microstructure comparable to that of the samples were sintered conventionally at 1550 °C.

In general, the external surface of the samples subjected to UHS exhibited no delaminations (Figure 3.24). Staircase effect was evident, like in all objects produced through AM. The sample whose holding time was 60 s revealed some inhomogeneities: as can be seen in image (b) of Figure 3.24, pores were concentrated at the junction between different layers. This was not the case for the samples with holding times of 300 s and 600 s, which confirms that a correct choice of process parameters is fundamental in order to achieve good results.

The external surface of the sample subjected to UHS for 600s was compared to that of a sample with the same original ink composition (56 vol.% alumina) but sintered through conventional methods. As

can be seen in Figure 3.25, the UHS sample displays big grains that are instead completely absent in the sample sintered conventionally. This unexpected microstructure is indicative of the fact that the surface reached an excessively high temperature during the UHS process, leading the sample very close to its melting temperature and possibly melting some impurities (according to the producer, the initial alumina powder contained 0.03% Na₂O, 0.04% MgO, 0.015% of Fe₂O₃, 0.015% of SiO₂ and 0.015% of CaO).

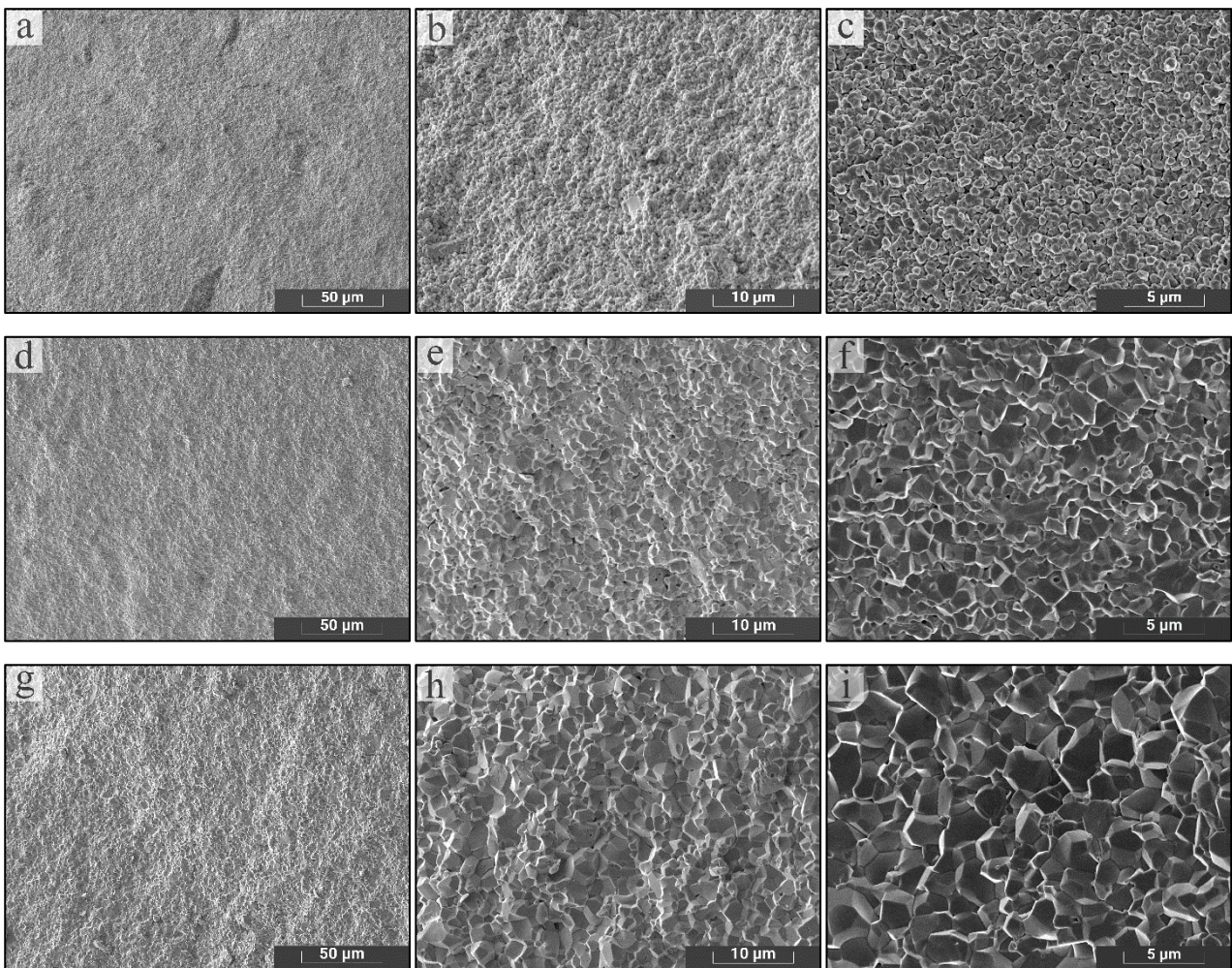


Figure 3.23: SEM micrographs showing the effect of the holding time during UHS on the microstructure of samples produced from the HDDA/PEGDA250-based ink with 56 vol.% alumina. The samples underwent UHS (9A) for different times: 60 s (a, b, c), 300 s (d, e, f) and 600 s (g, h, i).

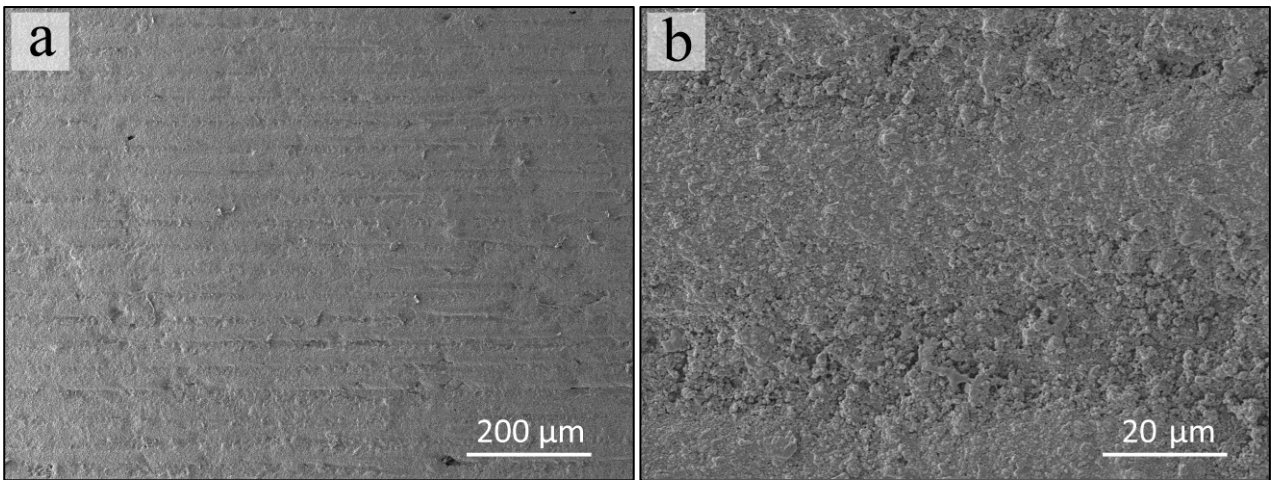


Figure 3.24: a) SEM image of the typical external surface of a sample subjected to UHS. b) Detail of the external surface of the sample subjected to UHS with a holding time of 60 s. Porosities are not distributed homogeneously and are concentrated in the points where different layers are joined together.

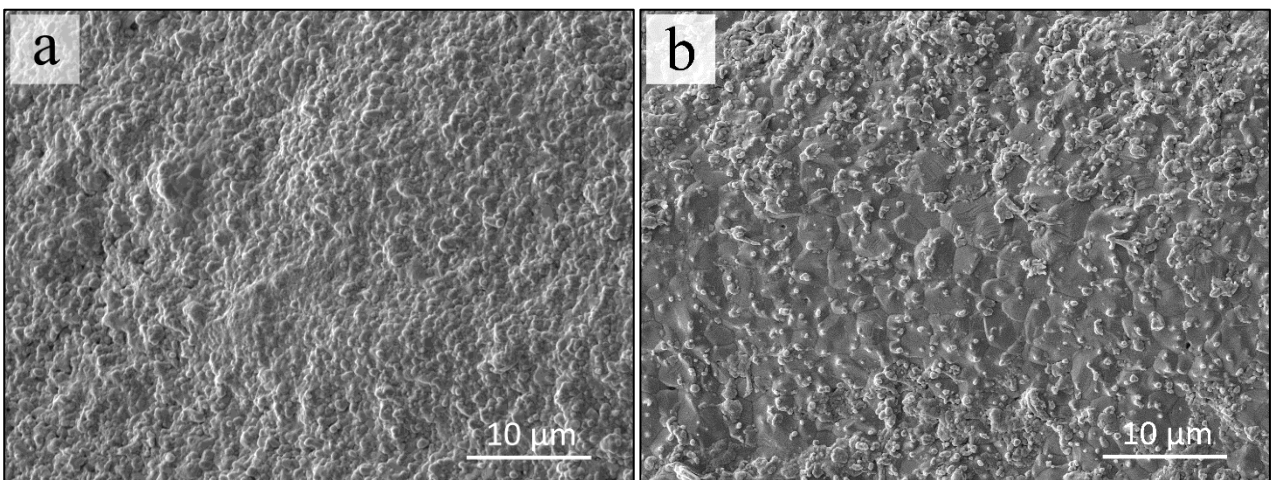


Figure 3.25: External surfaces of two samples derived from an HDDA/PEGDA250-based ink with 56 vol.% alumina. a) Sample sintered conventionally at 1550 °C for 1h. b) Sample consolidated through UHS with a holding time of 600 s.

The importance of the debinding step was verified by attempting to directly consolidate a green sample through UHS. The sample did not survive the experiment (Figure 3.26), proving that the removal of the organic fraction is necessary to prevent the formation of defects and the eventual structural collapse of the ceramic part. As mentioned in Chapter 1 and verified through the TGA, when temperature increases the binder starts to volatilize and eventually is pyrolyzed, generating hot

gases that have to be expelled from the structure. If they remain trapped, they generate a pressure that leads to the formation of porosities and even cracks in the body. This is amplified by UHS due to the very short times typical of this technology: the extremely fast heating rate causes the rapid formation and expansion of these gases, which have no time to try to diffuse towards the outside and apply a high stress to the structure, bringing it to failure.

While the benefits of UHS would be more pronounced if thermal debinding and sintering could be combined into a single step, eliminating the need for a separate debinding process, this approach is not feasible in our case due to the high binder content. However, extrusion-based methods like direct ink writing or fused filament fabrication offer a distinct advantage in this regard, as they enable faster debinding and sintering while maintaining the integrity of the printed structure.



Figure 3.26: Fragments of a green sample subjected directly to UHS without intermediate debinding step. The sample did not survive the process.

Conclusion

In this work, alumina components were fabricated using vat photopolymerization starting from an ink consisting of HDDA/PEGDA 250 as monomer, bis(2,4,6-trimethylbenzoyl)phenylphosphine oxide as photoinitiator, BYK-111 as dispersant and camphor as diluent. A maximum ceramic loading of 56 vol.% was found to be suitable for printing with a Prusa SL1S SPEED printer. The use of camphor was very beneficial in terms of reducing viscosity and particularly more prominent for higher ceramic loading. The debinded samples were UHSed and then exhibited similar (or even better) properties in terms of densification and microstructure when compared to the samples processed conventionally. The samples retained the same phase as the initial powder after the UHS process. These results suggest that combining innovative rapid sintering techniques with additive manufacturing represents the future of ceramic processing, paving the way for greener and more sustainable practices.

Outlook

While this work successfully produced an ink formulation for the fabrication of dense alumina parts through vat photopolymerization, some challenges still remain.

The green bodies displayed some surface delaminations only detectable through SEM. These defects are unwanted because they might survive the thermal treatments and remain in the final sintered objects, lowering the quality of the product. It is necessary to find the exact cause of these delaminations in order to prevent their formation.

The compatibility of VP and UHS was verified over the course of this study and samples of good quality were obtained, but the process parameters of UHS were far from optimized. In-depth analysis of the effect of different holding times and even different maximum power would allow to further improve the quality of the produced ceramic parts.

Another possible development of the findings of this work could be to study the mechanical properties of the samples in relation to their microstructure and process parameters, in order to determine the best ones.

Bibliography

- [1] Y. Lakhdar, C. Tuck, J. Binner, A. Terry, and R. Goodridge, “Additive manufacturing of advanced ceramic materials,” Feb. 01, 2021, *Elsevier Ltd.* doi: 10.1016/j.pmatsci.2020.100736.
- [2] C. Barry Carter and Grant Norton M., *Ceramic Materials: Science and Engineering*, First edition. Springer, 2007.
- [3] L. Yang and H. Miyanaji, “Ceramic additive manufacturing: a review of current status and challenges,” 2017.
- [4] M. Biesuz, S. Grasso, and V. M. Sglavo, “What’s new in ceramics sintering? A short report on the latest trends and future prospects,” *Curr Opin Solid State Mater Sci*, vol. 24, no. 5, Oct. 2020, doi: 10.1016/j.cossms.2020.100868.
- [5] Z. Chen *et al.*, “3D printing of ceramics: A review,” Apr. 01, 2019, *Elsevier Ltd.* doi: 10.1016/j.jeurceramsoc.2018.11.013.
- [6] “ISO/ASTM 52900:2021(en), Additive manufacturing — General principles — Fundamentals and vocabulary,” 2021, *ASTM International*. Accessed: Sep. 25, 2024. [Online]. Available: <https://www.iso.org/standard/74514.html>
- [7] R. Chaudhary, P. Fabbri, E. Leoni, F. Mazzanti, R. Akbari, and C. Antonini, “Additive manufacturing by digital light processing: a review,” Apr. 01, 2023, *Springer Science and Business Media Deutschland GmbH*. doi: 10.1007/s40964-022-00336-0.
- [8] M. Gebler, A. J. M. Schoot Uiterkamp, and C. Visser, “A global sustainability perspective on 3D printing technologies,” *Energy Policy*, vol. 74, no. C, pp. 158–167, 2014, doi: 10.1016/j.enpol.2014.08.033.
- [9] I. L. de Camargo, M. M. Morais, C. A. Fortulan, and M. C. Branciforti, “A review on the rheological behavior and formulations of ceramic suspensions for vat photopolymerization,” *Ceram Int*, vol. 47, no. 9, pp. 11906–11921, May 2021, doi: 10.1016/j.ceramint.2021.01.031.
- [10] C. E. Corcione, A. Greco, F. Montagna, A. Licciulli, and A. Maffezzoli, “Silica moulds built by stereolithography.”

- [11] H. I. Hsiang, C. Y. Lee, C. C. Chen, J. Wang, D. Tang, and Z. Dong, “Polycrystalline alumina ceramic fabrication using digital stereolithographic light process,” *Ceram Int*, vol. 47, no. 23, pp. 33815–33826, Dec. 2021, doi: 10.1016/j.ceramint.2021.08.293.
- [12] Q. Gu, H. Wang, W. Gao, J. Yu, and X. Zhou, “Preparation of large-size alumina ceramic parts by DLP 3D printing using high-solid-loading paste and optimizing the debinding process,” *Ceram Int*, vol. 49, no. 17, pp. 28801–28812, Sep. 2023, doi: 10.1016/j.ceramint.2023.06.142.
- [13] R. Erbereli, I. L. de Camargo, M. M. Morais, and C. A. Fortulan, “3D printing of trabecular bone-mimetic structures by vat photopolymerization of bovine hydroxyapatite as a potential candidate for scaffolds,” *Journal of the Brazilian Society of Mechanical Sciences and Engineering*, vol. 44, no. 5, May 2022, doi: 10.1007/s40430-022-03468-0.
- [14] R. He *et al.*, “Fabrication of complex-shaped zirconia ceramic parts via a DLP-stereolithography-based 3D printing method,” *Ceram Int*, vol. 44, no. 3, pp. 3412–3416, Feb. 2018, doi: 10.1016/j.ceramint.2017.11.135.
- [15] J. Schmidt and P. Colombo, “Digital light processing of ceramic components from polysiloxanes,” *J Eur Ceram Soc*, vol. 38, no. 1, pp. 57–66, Jan. 2018, doi: 10.1016/j.jeurceramsoc.2017.07.033.
- [16] Z. Chen *et al.*, “Fabrication of broadband wave-transparent Si₃N₄ ceramics with octet-truss lattice structure by vat photopolymerization 3D printing technology,” *J Eur Ceram Soc*, vol. 44, no. 4, pp. 2026–2036, Apr. 2024, doi: 10.1016/j.jeurceramsoc.2023.11.035.
- [17] M. Carve and D. Wlodkovic, “3D-printed chips: Compatibility of additive manufacturing photopolymeric substrata with biological applications,” Feb. 23, 2018, *MDPI AG*. doi: 10.3390/mi9020091.
- [18] S. Mamatha, P. Biswas, and R. Johnson, “Digital light processing of ceramics: an overview on process, materials and challenges,” Oct. 01, 2023, *Springer Science and Business Media Deutschland GmbH*. doi: 10.1007/s40964-022-00379-3.
- [19] S. Zakeri, M. Vippola, and E. Levänen, “A comprehensive review of the photopolymerization of ceramic resins used in stereolithography,” Oct. 01, 2020, *Elsevier B.V.* doi: 10.1016/j.addma.2020.101177.
- [20] J. A. Lewis, “Colloidal processing of ceramics,” *Journal of the American Ceramic Society*, vol. 83, no. 10, pp. 2341–2359, 2000, doi: 10.1111/j.1151-2916.2000.tb01560.x.

- [21] M. C. Newstein *et al.*, “Microstructural changes in a colloidal liquid in the shear thinning and shear thickening regimes,” *Journal of Chemical Physics*, vol. 111, no. 10, pp. 4827–4838, Sep. 1999, doi: 10.1063/1.479245.
- [22] K. Zhang *et al.*, “Photosensitive ZrO₂ suspensions for stereolithography,” *Ceram Int*, vol. 45, no. 9, pp. 12189–12195, Jun. 2019, doi: 10.1016/j.ceramint.2019.03.123.
- [23] X. Huang, H. Dai, Y. Hu, P. Zhuang, Z. Shi, and Y. Ma, “Development of a high solid loading β -TCP suspension with a low refractive index contrast for DLP -based ceramic stereolithography,” *J Eur Ceram Soc*, vol. 41, no. 6, pp. 3743–3754, Jun. 2021, doi: 10.1016/j.jeurceramsoc.2020.12.047.
- [24] F. Gao, S. Yang, P. Hao, and J. R. G. Evans, “Suspension stability and fractal patterns: A comparison using hydroxyapatite,” *Journal of the American Ceramic Society*, vol. 94, no. 3, pp. 704–712, Mar. 2011, doi: 10.1111/j.1551-2916.2010.04149.x.
- [25] C. J. Bae and J. W. Halloran, “Concentrated suspension-based additive manufacturing – viscosity, packing density, and segregation,” *J Eur Ceram Soc*, vol. 39, no. 14, pp. 4299–4306, Nov. 2019, doi: 10.1016/j.jeurceramsoc.2019.05.034.
- [26] S. Y. Song, M. S. Park, D. Lee, J. W. Lee, and J. S. Yun, “Optimization and characterization of high-viscosity ZrO₂ ceramic nanocomposite resins for supportless stereolithography,” *Mater Des*, vol. 180, Oct. 2019, doi: 10.1016/j.matdes.2019.107960.
- [27] X. Pan, M. A. Tasdelen, J. Laun, T. Junkers, Y. Yagci, and K. Matyjaszewski, “Photomediated controlled radical polymerization,” Nov. 01, 2016, *Elsevier Ltd.* doi: 10.1016/j.progpolymsci.2016.06.005.
- [28] Y. Yagci, S. Jockusch, and N. J. Turro, “Photoinitiated polymerization: Advances, challenges, and opportunities,” Aug. 10, 2010. doi: 10.1021/ma1007545.
- [29] J. D. Schofield, “Extending the boundaries of dispersant technology,” 2002.
- [30] J. W. Halloran, “Freeform Fabrication of Ceramics Via Stereolithography,” 1996. [Online]. Available: <https://www.researchgate.net/publication/279891733>
- [31] M. Pfaffinger, G. Mitteramskogler, R. Gmeiner, and J. Stampfl, “Thermal debinding of ceramic-filled photopolymers,” in *Materials Science Forum*, Trans Tech Publications Ltd, 2015, pp. 75–81. doi: 10.4028/www.scientific.net/MSF.825-826.75.

- [32] Y. H. Lee, J. Bin Lee, W. Y. Maeng, Y. H. Koh, and H. E. Kim, “Photocurable ceramic slurry using solid camphor as novel diluent for conventional digital light processing (DLP) process,” *J Eur Ceram Soc*, vol. 39, no. 14, pp. 4358–4365, Nov. 2019, doi: 10.1016/j.jeurceramsoc.2019.05.069.
- [33] E. Schwarzer, M. Götz, D. Markova, D. Stafford, U. Scheithauer, and T. Moritz, “Lithography-based ceramic manufacturing (LCM) – Viscosity and cleaning as two quality influencing steps in the process chain of printing green parts,” *J Eur Ceram Soc*, vol. 37, no. 16, pp. 5329–5338, Dec. 2017, doi: 10.1016/j.jeurceramsoc.2017.05.046.
- [34] Z. Xing, H. Zhou, W. Liu, J. Nie, Y. Chen, and W. Li, “Efficient cleaning of ceramic green bodies with complex architectures fabricated by stereolithography-based additive manufacturing via high viscoelastic paste,” *Addit Manuf*, vol. 55, Jul. 2022, doi: 10.1016/j.addma.2022.102809.
- [35] E. Johansson, O. Lidström, J. Johansson, O. Lyckfeldt, and E. Adolfsson, “Influence of resin composition on the defect formation in alumina manufactured by stereolithography,” *Materials*, vol. 10, no. 2, 2017, doi: 10.3390/ma10020138.
- [36] C. Riccio *et al.*, “Effects of Curing on Photosensitive Resins in SLA Additive Manufacturing,” *Applied Mechanics*, vol. 2, no. 4, p. 0, Dec. 2021, doi: 10.3390/applmech2040055.
- [37] S. Kirby, I. Pesun, A. Nowakowski, and R. França, “Effect of Different Post-Curing Methods on the Degree of Conversion of 3D-Printed Resin for Models in Dentistry,” *Polymers (Basel)*, vol. 16, no. 4, Feb. 2024, doi: 10.3390/polym16040549.
- [38] L. Zhang *et al.*, “Effects of debinding condition on microstructure and densification of alumina ceramics shaped with photopolymerization-based additive manufacturing technology,” *Ceram Int*, vol. 48, no. 10, pp. 14026–14038, May 2022, doi: 10.1016/j.ceramint.2022.01.288.
- [39] O. Santoliquido, F. Camerota, and A. Ortona, “The influence of topology on DLP 3D printing, debinding and sintering of ceramic periodic architectures designed to replace bulky components,” *Open Ceramics*, vol. 5, Mar. 2021, doi: 10.1016/j.oceram.2021.100059.
- [40] K. Wang *et al.*, “Study on defect-free debinding green body of ceramic formed by DLP technology,” *Ceram Int*, vol. 46, no. 2, pp. 2438–2446, Feb. 2020, doi: 10.1016/j.ceramint.2019.09.237.
- [41] M. N. Rahaman, *Ceramic Processing and Sintering*, Second edition. CRC Press, 2003.

- [42] Alima Carlos Averú, Luciano Volcanoglo Biehl, Jorge Luiz Braz Medeiros, and José De Souza, “Comparative Study of the Diffusibility of a Nickel Alloy composed by Ni - Cr - Fe,” *International Journal of Engineering Research and*, vol. V5, no. 12, Dec. 2016, doi: 10.17577/IJERTV5IS120261.
- [43] C. Wang *et al.*, “A general method to synthesize and sinter bulk ceramics in seconds,” *Science (1979)*, no. 368, May 2020, [Online]. Available: <https://www.science.org>
- [44] S. Bhandari *et al.*, “Ultra-rapid debinding and sintering of additively manufactured ceramics by ultrafast high-temperature sintering,” *J Eur Ceram Soc*, vol. 44, no. 1, pp. 328–340, Jan. 2024, doi: 10.1016/j.jeurceramsoc.2023.08.040.
- [45] K. Zhang, Q. Meng, Z. Qu, and R. He, “A review of defects in vat photopolymerization additive-manufactured ceramics: Characterization, control, and challenges,” Mar. 01, 2024, *Elsevier Ltd*. doi: 10.1016/j.jeurceramsoc.2023.10.067.
- [46] J. Schmidt, A. A. Altun, M. Schwentenwein, and P. Colombo, “Complex mullite structures fabricated via digital light processing of a preceramic polysiloxane with active alumina fillers,” *J Eur Ceram Soc*, vol. 39, no. 4, pp. 1336–1343, Apr. 2019, doi: 10.1016/j.jeurceramsoc.2018.11.038.
- [47] X. Xu, S. Zhou, J. Wu, C. Zhang, and X. Liu, “Inter-particle interactions of alumina powders in UV-curable suspensions for DLP stereolithography and its effect on rheology, solid loading, and self-leveling behavior,” *J Eur Ceram Soc*, vol. 41, no. 4, pp. 2763–2774, Apr. 2021, doi: 10.1016/j.jeurceramsoc.2020.12.004.
- [48] J. Sun, J. Binner, and J. Bai, “Effect of surface treatment on the dispersion of nano zirconia particles in non-aqueous suspensions for stereolithography,” *J Eur Ceram Soc*, vol. 39, no. 4, pp. 1660–1667, Apr. 2019, doi: 10.1016/j.jeurceramsoc.2018.10.024.
- [49] “Image source: Official website of Merck KGaA.” Accessed: Sep. 25, 2024. [Online]. Available: <https://www.sigmaaldrich.com/IT/en>
- [50] “Image source: Wikipedia entry for Camphor.” Accessed: Sep. 25, 2024. [Online]. Available: <https://it.wikipedia.org/wiki/Canfora>
- [51] A. M. Abyzov, “Aluminum Oxide and Alumina Ceramics (review). Part 1. Properties of Al₂O₃ and Commercial Production of Dispersed Al₂O₃,” *Refractories and Industrial Ceramics*, vol. 60, no. 1, pp. 24–32, May 2019, doi: 10.1007/s11148-019-00304-2.

- [52] H. S. Kim, N. K. Park, T. J. Lee, M. H. Um, and M. Kang, "Preparation of nanosized α - Al₂O₃ particles using a microwave pretreatment at mild temperature," *Advances in Materials Science and Engineering*, vol. 2012, 2012, doi: 10.1155/2012/920105.
- [53] A. A. Mohammed, Z. T. Khodair, and A. A. Khadom, "Preparation and investigation of the structural properties of α -Al₂O₃ nanoparticles using the sol-gel method," *Chemical Data Collections*, vol. 29, Oct. 2020, doi: 10.1016/j.cdc.2020.100531.
- [54] S. Kumar, V. D. Mote, R. Prakash, and V. Kumar, "X-ray Analysis of α -Al₂O₃ Particles by Williamson–Hall Methods," *Materials Focus*, vol. 5, no. 6, pp. 545–549, Nov. 2016, doi: 10.1166/mat.2016.1345.
- [55] K. R. Kambale, A. Mahajan, and S. P. Butee, "Effect of grain size on the properties of ceramics," *Metal Powder Report*, vol. 74, no. 3, pp. 130–136, May 2019, doi: 10.1016/j.mprp.2019.04.060.